STOCKHOLM UNIVERSITY

Doctoral Studies in Physics

Licensiate Thesis

Search for in Mono-jet Final States with the ATLAS Experiment

Advisor:
dott. Christophe Clement

Co-Supervisor:
dott. David Milstead

Candidate:
Gabriele Bertoli

December 12, 2015

Acknowledgments

Contents

List of Tables

List of Figures

Si sta,
come d'autunno,
sugli alberi,
le foglie

[G. UNGARETTI, Soldati]

Introduction

Chapter 1

Theoretical overview

1.1 The Standard Moldel of particle physics

1.2 The Standard Model

The *Standard Model* (SM) is a theoretical model which describes the elementary constituents of matter and their interactions. Up to now, we discovered four kind of different interactions, the *electromagnetic*, the *gravitational*, the *strong* and the *electro-weak interaction*; excluding gravity, all of them are described by means of a *quantum field gauge theory*.

The Standard Model is the collection of these gauge theories, it is based on the gauge symmetry group $SU(3)_C \times SU(2)_L \times U(1)_Y$ where $SU(3)_C$ is the symmetry group of the *Quantum Chromo-Dynamics* (QCD), the "C" subscript stand for *color charge* which is the conserved charge in the strong interaction. The $SU(2)_L$ is the weak isotopic spin group acting on *left-handed* doublet of fermions while the $U(1)_Y$ group is the *hypercharge* symmetry group of the *right-handed* fermion singlets. Together $SU(2)_L \times U(1)_Y$ form the electro-weak symmetry group.

The Standard Model also contains and (sometimes) predicts the existence of *elementary particles* that interacts between them via the forces mentioned above. The matter constituents are called *fermions*, the interaction are mediated by other particles called *gauge bosons*. Fermions are further categorized into *quark* and *leptons* and are the true fundamental constituents of matter; the gauge bosons arise by means of symmetry property of the Standard Model symmetry group.

The existence of all the leptons, quarks and gauge bosons is confirmed by experimental tests. Among the bosons, the Higgs boson is peculiar because, unlike the others, it is not associated with any interaction, instead is postulated as a consequence of the *spontaneously broken symmetry* of the electroweak sector which is the property, responsible of giving mass to all the elementary particles and the weak gauge bosons.

1.2.1 Electro-Weak Symmetry Group

We can now see how to find out the weak interaction symmetry group, to this end, let us start by writing out the *Hamiltonian*

$$H_{weak} = \frac{4G_F}{\sqrt{2}} J_\mu^\dagger J^\mu \tag{1.2.1}$$

where

$$
\begin{aligned}
J_\mu \equiv J_\mu^{(+)} &= \bar{\psi}_{\nu_e}\gamma_\mu \frac{1}{2}(1-\gamma_5)\psi_e \equiv \bar{\nu}_{e_L}\gamma_\mu e_L \\
J_\mu^\dagger \equiv J_\mu^{(-)} &= \bar{\psi}_e\gamma_\mu \frac{1}{2}(1-\gamma_5)\psi_{\nu_e} \equiv \bar{e}_L\gamma_\mu \nu_{e_L}
\end{aligned}
\tag{1.2.2}
$$

to easy the notation, let us write

$$
\chi_L = \begin{pmatrix} \nu_{e_L} \\ e_L^- \end{pmatrix} \equiv \begin{pmatrix} \nu_e \\ e^- \end{pmatrix}
\tag{1.2.3}
$$

and using the Pauli matrices

$$
\tau_\pm = \frac{1}{2}(\tau_1 \pm i\tau_2)
\tag{1.2.4}
$$

we have

$$
\begin{aligned}
J_\mu^{(+)} &= \bar{\chi}_L\gamma_\mu\tau_+\chi_L \\
J_\mu^{(-)} &= \bar{\chi}_L\gamma_\mu\tau_-\chi_L
\end{aligned}
\tag{1.2.5}
$$

by introducing a “neutral” current

$$
J_\mu^{(3)} = \bar{\chi}_L\gamma_\mu\frac{\tau_3}{2}\chi_L = \frac{1}{2}\bar{\nu}_L\gamma_\mu\nu_L - \frac{1}{2}\bar{e}_L\gamma e_L
\tag{1.2.6}
$$

we have a “triplet” of currents

$$
J_\mu^i = \bar{\chi}_L\gamma_\mu\frac{\tau_i}{2}\chi_L.
\tag{1.2.7}
$$

Now if we pick up an $SU(2)_L$ transformation

$$
\chi_L(x) \to \chi_L'(x) = e^{i\vec{\varepsilon}\cdot\vec{T}}\chi_L(x) = e^{i\vec{\varepsilon}\cdot\frac{\vec{\tau}}{2}}\chi_L(x),
\tag{1.2.8}
$$

where $T_i = \tau_i/2$ are the $SU(2)_L$ *generators*, and think the χ_L as the *fundamental representation*, then the current triplet is a triplet of $SU(2)_L$, the *weak isotopic spin*.

The right handed fermions are singlet for the $SU(2)_L$, thus

$$
e_R \to e_R' = e_R.
\tag{1.2.9}
$$

Since we are considering the global transformations, we have no interaction, so the Lagrangian reads

$$
\mathcal{L} = \bar{e}i\gamma^\mu\partial_\mu e + \bar{\nu}i\gamma^\mu\partial_\mu\nu \equiv \bar{\chi_L}i\gamma\partial\chi_L + \bar{e}_R i\gamma\partial e_R;
\tag{1.2.10}
$$

for now we are bounded to set $m_e = 0$, in fact the mass term couples right and left fermion’s components and it is not $SU(2)_L$ invariant. In 1973, experiments detected events of the type

$$
\bar{\nu}_\mu e^- \to \bar{\nu}_\mu e^-
\tag{1.2.11}
$$

$$
\begin{cases}
\nu_\mu N \to \nu_\mu X \\
\bar{\nu}_\mu N \to \bar{\nu}_\mu X
\end{cases}
\tag{1.2.12}
$$

which are evidence of a neutral current. Further investigations yielded that the neutral weak current is predominantly $V-A$ (i.e. left-handed) but not purely $V-A$ so the

$J_\mu^{(3)}(x)$ current introduced above can not be used as it involves only left handed fermions. We know a neutral current that mixes left and right components namely the electromagnetic current

$$J_\mu \equiv e J_\mu^{(em)} = e\bar{\psi}\gamma_\mu Q\psi \tag{1.2.13}$$

where Q is the charge operator with eigenvalue $Q = -1$ for the electron. Q is the generator of the $U(1)_{(em)}$ group. So we have an isospin triplet and we have included the right hand components, the isospin singlet, what we want to do, is to combine them and define the hypercharge operator

$$Y = 2(Q - T_3) \rightarrow Q = T_3 + \frac{Y}{2}, \tag{1.2.14}$$

for the current we have

$$J_\mu^{(em)} = J_\mu^{(3)} + \frac{1}{2}J_\mu^Y \tag{1.2.15}$$

where

$$J_\mu^Y = \bar{\psi}\gamma_\mu Y\psi \tag{1.2.16}$$

so, by analogy, the hypercharge Y generates a $U(1)_Y$ symmetry, and, as it is a $SU(2)_L$ singlet, leaves (1.2.10) invariant under the transformations

$$\begin{aligned} \chi_L(x) &\rightarrow \chi'_L(x) = e^{i\beta Y}\chi_L(x) \equiv e^{i\beta y_L}\chi_L \\ e_R(x) &\rightarrow e'_R(x) = e^{i\beta Y}e_R(x) \equiv e^{i\beta y_R}e_R. \end{aligned} \tag{1.2.17}$$

We thus have incorporated the electromagnetic interactions extending the group to $SU(2)_L \times U(1)_Y$ and instead of having a single symmetry group we have a direct product of groups, each with his own *coupling constant*, so, in addition to e we will have another coupling to be found. Since we have a direct product of symmetry groups, the generators of $SU(2)_L$, T_i, and the generators of $U(1)_Y$, Y commute, the commutation relations are

$$[T_+, T_-] = 2T_3 \quad ; \quad [T_3, T_\pm] = \pm T_\pm \quad ; \quad [Y, T_\pm] = [Y, T_3] = 0, \tag{1.2.18}$$

member of the same isospin triplet, have same hypercharge eigenvalue; the relevant quantum numbers are summarized in the table 1.1.

Lepton	T	$T^{(3)}$	Q	Y
ν_e	$\frac{1}{2}$	$\frac{1}{2}$	0	-1
e_L^-	$\frac{1}{2}$	$-\frac{1}{2}$	-1	-1
e_R^+	0	0	-1	-2

Quark	T	$T^{(3)}$	Q	Y
u_L	$\frac{1}{2}$	$\frac{1}{2}$	$\frac{2}{3}$	$\frac{1}{3}$
d_L	$\frac{1}{2}$	$-\frac{1}{2}$	$-\frac{1}{2}$	$\frac{1}{3}$
u_R	0	0	$\frac{2}{3}$	$\frac{4}{3}$
d_R	0	0	$-\frac{1}{3}$	$-\frac{2}{3}$

Table 1.1: Weak Isospin and Hypercharge Quantum Numbers of Leptons and Quarks

1.2.2 Electro-Weak Interactions

As stated before, interactions are mediated by a gauge boson, we now want to find out those for the electroweak interaction, to this end let us consider *local* gauge transformations

$$\begin{aligned} \chi_L &\rightarrow \chi'_L = e^{i\vec{\epsilon}(x)\cdot\vec{T} + i\beta(x)Y}\chi_L \\ \psi_R &\rightarrow \psi'_R = e^{i\beta(x)Y}\psi_R, \end{aligned} \tag{1.2.19}$$

introducing four gauge bosons, $W_\mu^{(1)}, W_\mu^{(2)}, W_\mu^{(3)}, B_\mu$ (same as the number of generators) and the *covariant derivative*

$$\begin{aligned} D_\mu\chi_L &= (\partial_\mu + ig\frac{\vec{\tau}}{2}\cdot\overrightarrow{W}_\mu(x) + i\frac{g'}{2}y_L B_\mu(x))\chi_L \\ &= (\partial_\mu + ig\frac{\vec{\tau}}{2}\cdot\overrightarrow{W}_\mu(x) - i\frac{g'}{2}B_\mu(x))\chi_L \\ D_\mu\psi_R &= (\partial_\mu + i\frac{g'}{2}y_R B_\mu(x))\psi_R \\ &= (\partial_\mu - i\frac{g'}{2}B_\mu(x))e_R \end{aligned} \tag{1.2.20}$$

the Lagrangian (1.2.10) reads

$$\begin{aligned} \mathcal{L} = &\bar{\chi}_L i\gamma\partial\chi_L + \bar{e}_R i\gamma\partial e_R - g\bar{\chi}_L\gamma^\mu\frac{\vec{\tau}}{2}\chi_L\overrightarrow{W}_\mu + \frac{g'}{2}(\bar{\chi}_L\gamma^\mu\chi_L + 2\bar{e}_R\gamma^\mu e_R)B_\mu \\ &- \frac{1}{4}\overrightarrow{W}_{\mu\nu}\overrightarrow{W}^{\mu\nu} - \frac{1}{4}B_{\mu\nu}B^{\mu\nu} \end{aligned} \tag{1.2.21}$$

where

$$\begin{aligned} \overrightarrow{W}_{\mu\nu} &= \partial_\mu\overrightarrow{W}_\nu - \partial_\nu\overrightarrow{W}_\nu - g\overrightarrow{W}_\mu \times \overrightarrow{W}_\nu \\ B_{\mu\nu} &= \partial_\mu B_\nu - \partial_\nu B_\nu \end{aligned} \tag{1.2.22}$$

are the kinetic plus non abelian interaction term for the $SU(2)_L$ symmetry (first equation) and the kinetic term for the abelian symmetry group $U(1)_Y$. We can now split the Lagrangian terms to find out the field of the vector bosons coupled to the charged current and to the neutral current.

Charged Currents Interaction Let us consider the term

$$\mathcal{L}_{int}^{ew} = -g\bar{\chi}_L\gamma_\mu\frac{\vec{\tau}}{2}\chi_L\overrightarrow{W}_\mu + \frac{g'}{2}\bar{\chi}_L\gamma_\mu\chi_L B^\mu + g'\bar{e_R}\gamma_\mu e_R B^\mu \tag{1.2.23}$$

defining

$$W_\mu^\pm = \frac{1}{\sqrt{2}}W^{(1)} \mp iW^{(2)} \tag{1.2.24}$$

we can write

$$\mathcal{L}^{CC} = -\frac{g}{\sqrt{2}}(J_\mu^{(+)}W^{-\mu} + J_\mu^{(-)}W^{+\mu}) \tag{1.2.25}$$

and recognize two charged vector bosons with coupling given by "g".

Neutral Current Interaction The relevant term left to consider for what concerns the electroweak currents is

$$\mathcal{L}^{NC} = -gJ_\mu^{(3)}W^{(3)\mu} - \frac{g'}{2}J_\mu^Y B^\mu, \tag{1.2.26}$$

the electromagnetic interaction, $-ieJ^{(em)\mu}A_\mu$, is embedded in this expression as will became clear considering the *spontaneously broken symmetry* phenomena, for now, is sufficient to define

$$\begin{aligned} W_\mu^{(3)} &= \cos\theta_w Z_\mu + \sin\theta_w A_\mu \\ B_\mu &= -\sin\theta_w Z_\mu + \cos\theta_w A_\mu \end{aligned} \tag{1.2.27}$$

and invert to get

$$\begin{aligned} A_\mu &= \sin\theta_w W_\mu^{(3)} + \cos\theta_w B_\mu \\ Z_\mu &= \cos\theta_w W_\mu^{(3)} - \sin\theta_w B_\mu \end{aligned} \tag{1.2.28}$$

where θ_w is the electroweak *mixing angle*. Plugging this into (1.2.26) and rearranging terms

$$\begin{aligned} \mathcal{L}^{NC} = &-[(g\sin\theta_w J_\mu^{(3)} + \frac{g'}{2}\cos\theta_w J_\mu^Y)A^\mu \\ &+ (g\cos\theta_w J_\mu^{(3)} - \frac{g'}{2}\sin\theta_w J_\mu^Y)Z^\mu] \end{aligned} \tag{1.2.29}$$

since A^μ is the photon field, the first parenthesis must be identified with the electromagnetic current, thus

$$-(g\sin\theta_w J_\mu^{(3)} + \frac{g'}{2}\cos\theta_w J_\mu^Y)A^\mu = -eJ_\mu^{(em)}A^\mu \equiv -e(J_\mu^{(3)} + \frac{J_\mu^Y}{2})A^\mu \tag{1.2.30}$$

from which we get the relation

$$g\sin\theta_w = g'\cos\theta_w = e \tag{1.2.31}$$

and so we can rewrite (1.2.26),

$$\mathcal{L}^{NC} = -\frac{g}{\cos\theta_w}[J_\mu^{(3)} - \sin^2\theta_w J_\mu^{(em)}]Z^\mu \tag{1.2.32}$$

so that Z^μ can be identified with the field for the neutral vector boson.

1.3 The Higgs mechanism

Up to now, we have massless gauge vector bosons, in fact no term such as $M^2 B_\mu B^\mu/2$ appear in the Lagrangian (1.2.21), but this kind of terms are not gauge invariant and thus we can not just add them or we will end up with troubles later when trying to renormalize the theory.

A gauge invariant way to recover the fermions and bosons masses, is to spontaneously brake the local $SU(2)_L \times U(1)_Y$ electroweak symmetry.

1.3.1 Non Abelian Spontaneously Broken Symmetry

Let us consider a local symmetry breaking and refer to [1] for a more complete explanation. Be ϕ a complex scalar field,

$$\mathcal{L} = (\partial_\mu\phi^*)(\partial_\mu\phi) - \underbrace{\mu^2\phi^*\phi - \lambda(\phi^*\phi)^2}_{V(\phi^*\phi)} \tag{1.3.1}$$

setting

$$\begin{aligned} \phi &= \frac{\phi_1 + i\phi_2}{\sqrt{2}} \\ \phi^* &= \frac{\phi_1 - i\phi_2}{\sqrt{2}} \end{aligned} \tag{1.3.2}$$

we get

$$\mathcal{L} = \frac{1}{2}(\partial_\mu \phi_1)^2 + \frac{1}{2}(\partial_\mu \phi_2)^2 - \frac{\mu^2}{2}(\phi_1^2 + \phi_2^2) - \frac{\lambda}{4}(\phi_1^2 + \phi_2^2)^2 \tag{1.3.3}$$

the gauge transformations are

$$\begin{cases} \phi\ (x) \to \phi\ '(x) = e\ \ ^{i\epsilon}\phi\ (x) \\ \phi^\dagger(x) \to \phi^{\dagger\prime}(x) = e^{-i\epsilon}\phi^\dagger(x). \end{cases} \tag{1.3.4}$$

There are two possible choices for the potential

- $\mu^2 > 0$, which gives a stable configuration around $|\phi| = 0$.
- $\mu^2 < 0$, which gives a circle of minima such that $\phi_1^2 + \phi_2^2 = v^2$, with $v^2 = -\mu^2/\lambda$. This minima are not gauge invariant, in fact

$$\phi_0 = \langle 0|\phi|0\rangle \to \frac{v}{\sqrt{2}}e^{i\alpha} \quad \texttt{if} \quad \phi \to e^{i\alpha}\phi \tag{1.3.5}$$

To get the particle interaction we make a perturbative expansion around one minimum, we chose one, for example $\alpha = 0$, for which $\phi_1 = v$ and $\phi_2 = 0$ and introduce the two perturbations $\eta(x)$ and $\xi(x)$ so that

$$\phi(x) = \frac{1}{\sqrt{2}} \overbrace{v + \xi(x)}^{\phi_1} + i\overbrace{\eta(x)}^{\phi_2} \tag{1.3.6}$$

and plug them in the Lagrangian (1.3.3) to obtain

$$\begin{aligned} \mathcal{L}'(\xi, \eta) = &\frac{1}{2}(\partial_\mu \xi)^2 + \frac{1}{2}(\partial_\mu \eta)^2 - \frac{1}{2}(-2\mu^2)\eta^2 \\ &- \lambda v(\eta^2 + \xi^2)\eta - \frac{1}{4}(\eta^2 + \xi^2)^4 + \cdots \end{aligned} \tag{1.3.7}$$

as we can see, the third term looks like a mass term so that the field η has mass $m_\eta^2 = -2\mu^2$ while we have no mass term for the field ξ.

This "trick" to give mass to one of the gauge field, is the *braking of the symmetry*. In fact, by choosing one particular vacuum among the infinite ones, we lost our gauge invariance; moreover, we ended up with a scalar gauge boson, known as *Goldstone boson*. We need to find a way to recover the masses of the gauge bosons in a gauge invariant way by getting rid of massless scalar fields; the solution is the topic of the very next section. next section.

1.3.2 The Higgs Mechanism

Consider now a local gauge $SU(2)$ symmetry, the field transformations are

$$\phi(x) \to \phi'(x) = e^{i\sum_{k=1}^{3}\epsilon^k T^k}\phi(x), \tag{1.3.8}$$

where $T^k = \frac{\tau^k}{2}$ and $[T^i, T^j] = i\epsilon^{ijk}T^k$ with $i, j, k = 1,2,3$. To achieve invariance for the Lagrangian

$$\mathcal{L} = (\partial_\mu \phi)^\dagger(\partial^\mu \phi) - \mu^2\phi^\dagger\phi - \lambda(\phi^\dagger\phi)^2, \tag{1.3.9}$$

where

$$\phi \equiv \begin{pmatrix} \phi_i \\ \phi_j \end{pmatrix} = \frac{1}{\sqrt{2}}\begin{pmatrix} \phi_1 + i\phi_2 \\ \phi_3 + i\phi_4 \end{pmatrix}, \tag{1.3.10}$$

we need to introduce the covariant derivative

$$D_\mu = \partial_\mu + ig\,\tfrac{\vec{\tau}}{2}\cdot\overrightarrow{W}_\mu(x). \tag{1.3.11}$$

In the case of infinitesimal transformations, the fields transform like

$$\phi(x) \to \phi'(x) \simeq (1 + i\vec{\epsilon}(x)\cdot\tfrac{\vec{\tau}}{2})\phi(x) \tag{1.3.12}$$

while the gauge bosons transformations are

$$\overrightarrow{W}_\mu(x) \to \overrightarrow{W}_\mu(x) - \frac{1}{g}\partial_\mu\vec{\epsilon}(x) - \vec{\epsilon}(x)\times\overrightarrow{W}_\mu(x). \tag{1.3.13}$$

Replacing everything in the Lagrangian we obtain

$$\mathcal{L} = (\partial_\mu\phi + ig\,\tfrac{\vec{\tau}}{2}\cdot\overrightarrow{W}_\mu\phi)^\dagger(\partial_\mu\phi + ig\,\tfrac{\vec{\tau}}{2}\cdot\overrightarrow{W}_\mu) - V(\phi) - \frac{1}{4}\overrightarrow{W}_{\mu\nu}\cdot\overrightarrow{W}^{\mu\nu}, \tag{1.3.14}$$

where the potential is given by

$$V(\phi) = \mu^2\phi^\dagger\phi + \lambda(\phi^\dagger\phi)^2 \tag{1.3.15}$$

and the kinetic term is

$$\overrightarrow{W}_{\mu\nu} = \partial_\mu\overrightarrow{W}_\nu - \partial_\nu\overrightarrow{W}_\mu - g\,\overrightarrow{W}_\mu\times\overrightarrow{W}_\nu. \tag{1.3.16}$$

We are interested in the case of the spontaneously broken symmetry, thus $\mu^2 < 0$ and $\lambda > 0$. The minima of the potential lie on

$$\phi^\dagger\,\phi = \frac{1}{2}(\phi_1^2 + \phi_2^2 + \phi_3^2 + \phi_4^2) = -\frac{\mu^2}{2\lambda} \tag{1.3.17}$$

and we have to choose one of them, let it be

$$\phi_1 = \phi_2 = \phi_4 = 0, \quad \phi_3^2 = -\frac{\mu^2}{\lambda} \equiv v^2. \tag{1.3.18}$$

To expand ϕ around this particular vacuum

$$\phi_0 \equiv \frac{1}{\sqrt{2}}\begin{pmatrix}0\\ v\end{pmatrix} \tag{1.3.19}$$

it is sufficient to substitute the expansion

$$\phi(x) = \frac{1}{\sqrt{2}}\begin{pmatrix}0\\ v + h(x)\end{pmatrix} \tag{1.3.20}$$

in the Lagrangian (1.3.14) in order to get rid of the, unobserved, Goldstone bosons and retain only one neutral scalar field, the *Higgs field*.

1.3.3 Masses for the $W^{\pm}$ and Z^0 Gauge Bosons

The gauge bosons masses are generated simply substituting the vacuum expectation value, ϕ_0, in the Lagrangian, the relevant term is

$$\begin{aligned}
\left|(g\,\tfrac{\vec{\tau}}{2}\cdot\overrightarrow{W}_\mu+\tfrac{g'}{2}B_\mu)\phi\right|^2 = & \\
&= \frac{1}{8}\left|\begin{pmatrix} gW^3_\mu+g'B_\mu & g(W^1_\mu-iW^2_\mu) \\ g(W^1_\mu+iW^2_\mu) & -gW^3_\mu+g'B_\mu\end{pmatrix}\begin{pmatrix}0\\ v\end{pmatrix}\right|^2 \\
&= \frac{1}{8}v^2g^2[(W^1_\mu)^2+(W^2_\mu)^2]+\frac{1}{8}v^2(g'B_\mu-gW^3_\mu)(g'B^\mu-gW^{3\mu}) \\
&= (\frac{1}{2}gv)^2W^+_\mu W^{-\mu}+\frac{1}{8}v^2\begin{pmatrix}W^3_\mu & B_\mu\end{pmatrix}\begin{pmatrix} g^2 & -gg' \\ -gg' & g^2\end{pmatrix}\begin{pmatrix}W^{3\mu}\\ B^\mu,\end{pmatrix}
\end{aligned} \tag{1.3.21}$$

having used $W^{\pm}=(W^1\mp iW^2)/\sqrt{2}$. The mass term, lead us to conclude that

$$M_W=\frac{1}{2}gv. \tag{1.3.22}$$

The remaining term is off diagonal

$$\begin{aligned}
\frac{1}{8}v^2[g^2(W^3_\mu)^2-2gg'W^3_\mu B^\mu+g'^2B^2_\mu] = & \frac{1}{8}v^2[gW^3_\mu-gB_\mu]^2 \\
& +0\quad [g'W^3_\mu-g'B_\mu]^2
\end{aligned} \tag{1.3.23}$$

but one can diagonalize and find that

$$\begin{aligned}
A^\mu &= \frac{g'W^3_\mu+gB_\mu}{\sqrt{g^2+g'^2}} \\
Z^\mu &= \frac{gW^3_\mu+g'B_\mu}{\sqrt{g^2+g'^2}}
\end{aligned} \tag{1.3.24}$$

with $M_A=0$ and $M_Z=v\sqrt{g^2+g'^2}/2$ which are the photon and neutral weak vector boson fields. Thus the mass eigenstates are a massless vector boson, A_μ and a massive gauge boson Z_μ.

We have shown in this section how the Higgs mechanism can be applied to give mass to the gauge bosons of the electroweak model.

1.4 The Hierarchy Problem and Naturalness

The *naturalness criterion* states that one such [dimensionless and measured in units of the cut-off] parameter is allowed to be much smaller than unity only if setting it to zero increases the symmetry of the theory. If this does not happen, the theory is unnatural [2].

There are two important concepts in physics that enter in the formulation of the naturalness principle, symmetries and effective field theories. *Symmetries* are closely connected to conservation laws, moreover theory parameters that are protected by a symmetry, if smaller than the unit, are not problematic according to the naturalness criterion. *Effective field theories* are a sort of simplification of a more general theory that use less parameters to describe the dynamics of particles with energies less than a cut-off scale Λ.

Let us now consider the strength of the gravitational force, characterized by the Newton's constant, G_N and the weak force, characterized by the Fermi's constant G_F, if we take the ratio of these we get:

$$\frac{G_F \hbar^2}{G_N c^2} = 1.738 \times 10^{33}. \tag{1.4.1}$$

The reason why this number is worth some attention is that theory parameters close to the order of the unit in the SM, may be calculated in a more fundamental theory, if any, using fundamental constants like π or e while very big numbers may not have such a simple mathematical expression and thus may lead to uncover new properties of the fundamental theory.

This number becomes even more interesting if we consider quantum effects. *Virtual particles* are not really particles but rather disturbances in a field, these disturbances are off-shell ($E \neq m^2 + p^2$) and according to the *uncertainty principle*, $\Delta t \Delta E \geq \hbar/2$, can appear out of nothing for a short time that depends on the energy of the virtual particle; according to quantum field theory, the vacuum is populated with such disturbances. The Higgs field, has the property to couple with other SM particles with a strength proportional to their mass. Now all these virtual particles have a mass determined by the available energy Λ and when the Higgs field travels through space, it couples with these virtual particles and, due to quantum corrections, its motion is affected and its invariant mass squared gets a contribution proportional to Λ:

$$\delta m_H^2 = k\Lambda^2, \text{ with } k = \frac{3G_F}{4\sqrt{2}\pi^2}(4m_t^2 - 2m_W^2 - m_Z^2 - m_H^2). \tag{1.4.2}$$

Since $k \approx 10^{-2}$[3], the value of Higgs' mass $m_H \sim G_F^{-1/2}$, should be close to the maximum energy scale Λ and if we assume this to be the Plank scale $M_{Pl} = G_N^{-1/2}$, the ration G_F/G_N, should be close to the unity which contradicts eq. (1.4.1), this goes by the name of *hierarchy problem*.

The large quantum corrections in (1.4.2) are mainly due to the fact that in the SM, there is no symmetry protecting the mass of the Higgs' field. Supersymmetry (SUSY), among other things, is capable of solving the hierarchy problem by canceling out the quantum corrections that bring m_H close to Λ thus restoring the naturalness of the SM.

Chapter 2

Experimental Apparatus

2.1 The Large Hadron Collider

The Large Hadron Collider (LHC) [4] is a two ring superconducting hadron accelerator and collider located at the European Organization for Nuclear Research (CERN).

The performance of a collider is evaluated in terms of its available *center of mass energy*, $\sqrt{s}$ and the *instantaneous luminosity* $\mathcal{L}$. The former defines the accessible phase space (the momenta) for the production of final state particles. The latter is defined as the interaction rate per unit cross section of the colliding beams (collisions / (cm^2 s)).

The LHC is designed to operate at $\sqrt{s} = 14$ TeV in the center of mass although it started off at 7 TeV in 2010 and 2011, 8 TeV in 2012 and 13 TeV in 2015 after the long shutdown between 2013 and 2014.

There are six experiments at LHC: ATLAS [5], CMS [6], ALICE, LHCb, LHCf and TOTEM. ATLAS and CMS aim to a peak luminosity of $L = 10^{34}$ cm^{-2} s^{-1}, this requirement exclude the use of anti-proton beams and therefore the LHC is designed to be a proton-proton (pp) collider. The protons are obtained by ionization of hydrogen atoms and organized in bunches, accelerated by LINAC2 to an energy of 50 MeV and subsequently injected in the Proton Synchrotron Booster (PSB). Here they are further accelerated to an energy of 1.4 GeV and fed to the Proton Synchrotron (PS) where they reach the energy of 25 GeV to be then passed to the Super Proton Synchrotron (SPS) which accelerate them to an energy of 450 GeV. They are finally injected in the LHC in opposite direction where they reach the nominal energy. There are four interaction points where the four main experiments (ATLAS, CMS, ALICE, LHCb) are located, at these locations, every 25 μs, the bunches cross and interact with each other (*bunch crossing*). A schematic view of the injection chain is depicted in Figure 2.1.

The instantaneous luminosity depends on the beam parameters and is given by:

$$\mathcal{L} = \frac{N_b^2 n_b f_{rev} \gamma}{4\pi \epsilon_n \beta^*} F \tag{2.1.1}$$

where N_b is the number of particles per bunch, n_b is the number of bunches per beam, f_{rev} is the revolution frequency, γ is the relativistic gamma factor, ϵ_n the normalized transverse beam emittance, the beta function is a measure of the transverse beam size and β^* is the value of the beta function at the interaction point and F is the geometric reduction factor due to the crossing angle of the beams at the interaction point (IP) [4]. The integrated luminosity is given by:

$$L = \int \mathcal{L} \mathrm{d}t \tag{2.1.2}$$

and the integral is carried over data taking periods of the detector. The integrated luminosity can be related to the total number of events by:

$$N_{events} = L\sigma_{events} \tag{2.1.3}$$

where N_{events} is the total number of events, L is the integrated luminosity and σ_{events} is the cross section of the events in units of barn (1 b = 10^{-24} m^2). In 2015 ATLAS recorded an integrated luminosity of 3.2 fb^{-1}.

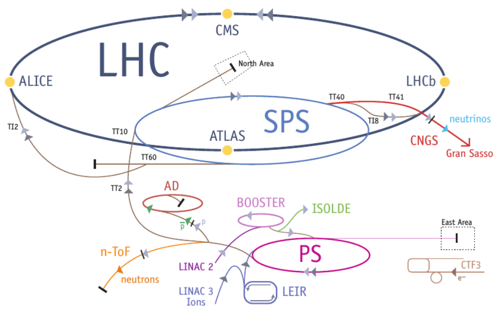

Figure 2.1: The LHC injection chain.

2.2 The ATLAS Detector

A Toroidal LHC apparatuS (ATLAS) is a multi purpose detector designed to be sensitive to a large physics signatures (supersymmetry, dark matter and extra dimensions) and to fully take advantage of the LHC potential. It is capable of identifying photons, electrons, muons, taus, jets and missing energy, Figure 2.2a shows a schematic view of the interaction of the different kind of particles with the ATLAS sub-detectors while Figure 2.2b shows the ATLAS detector with its subsystems. In the following sections a brief overview of the various system that allow particle identification and reconstruction is presented.

2.2.1 The Coordinate System

The ATLAS detector uses a right handed coordinate system with the origin at the nominal interaction point with the z-axis along the beam direction and the xy plane orthogonal to it. The positive x-axis goes from the interaction point to the center of the LHC ring and the positive y-axis is defined as pointing upwards. The A-side of the detector is defined as that with a positive z-axis while the C-side has the negative z-axis.

The LHC beam are unpolarized and thus invariant under rotations around the beam line axis, a cylindrical coordinate system is particularly convenient to describe the detector geometry where:

$$r = \sqrt{x^2 + y^2}, \quad \phi = \tan^{-1} \frac{y}{x}. \tag{2.2.1}$$

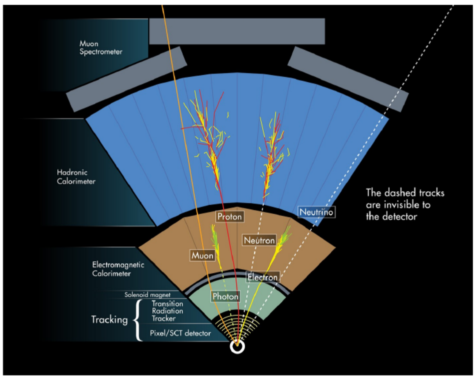

(a) Section of the ATLAS detector showing the interaction of different particles with the sub-detectors.

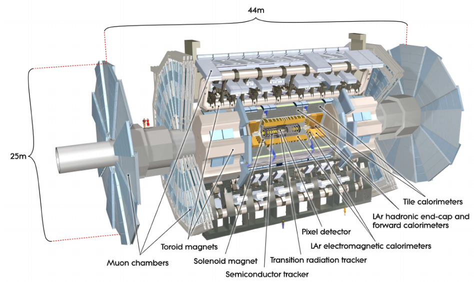

(b) Overview of the ATLAS detectors with its main sub-detectors.

Figure 2.2

A momentum dependent coordinate, the *rapidity*, is commonly used in particle physics for its properties under Lorentz transformations. The rapidity is defined as:

$$Y = \frac{1}{2} \ln \frac{E + p_z}{E - p_z} \tag{2.2.2}$$

where E is the energy of the particle and p_z its momentum along the z-axis. Rapidity interval are Lorentz invariant and in the relativistic limit or when the mass of the particle is negligible, the rapidity only depends on the production angle of the particle with respect to the beam axis,

$$\theta = \tan^{-1} \frac{r}{z}. \tag{2.2.3}$$

This approximation is called *pseudorapidity* (η) and is defined as:

$$Y \xrightarrow{p \gg m} \eta = -\ln \left(\tan \frac{\theta}{2} \right). \tag{2.2.4}$$

A value of $\theta = 90°$, perpendicular to the beam axis, corresponds to $\eta = 0$. The spatial separation between particles in the detector is commonly given in terms of a Lorentz invariant variable defined as:

$$\Delta R = \sqrt{\Delta\phi^2 + \Delta\eta^2}. \tag{2.2.5}$$

Other quantities used to describe the kinematics of the pp interaction are the *transverse momentum* (p_{T}) and the *transverse energy* (E_{T}) defined as $p_{\mathrm{T}} = p \sin\theta$ and $E_{\mathrm{T}} = E \sin\theta$ respectively.

2.2.2 The Inner Detector

The Inner Detector (ID) is designed to provide good track reconstruction, precise momentum resolution and both primary and secondary vertex measurements above a nominal p_{T} threshold of 0.5 GeV and within the pseudorapidity $|\eta| < 2.5$. It also provides electron identification over $|\eta| < 2.0$ for energies between 0.5 GeV and 150 GeV [5]. The ID is 6.2 m long and has a radius of about 1.1 m, it is surrounded by a solenoidal magnetic field of 2 T. Its layout is schematized in Figure 2.3 and, as can be seen, it is composed of three sub-detectors.

At the inner radius the *pixel detector* mostly determines the position of primary and secondary vertex. The silicon sensors are 250 μm thick detectors that operate with an initial bias voltage of $\sim$150 V that, due to the high radiation level, will increase up to 600 V after 10 years of operation to maintain a good charge collection.

In the middle layer of the ID the SemiConductor Tracker (SCT) is designed to give eight precision measurements per track which contributes to determine the primary and secondary vertex position and momentum measurements. The silicon sensors are 285 $\pm 15 \mu$m thick and initially operates with a bias voltage of $\sim$150 V which will increase up to 350 V after ten years of operation for good charge collection.

The last layer of the ID is the Transition Radiation Tracker (TRT), it contributes to tracking and identification of charged particles. It consists of drift (straw) tubes, 4 mm in diameter with a 31 μm wire in the center of each straw, filled with a gas mixture of 70% Xe, 27% CO_2 and 3% O_2. These tubes substantially act like proportional counters where the tube is the cathode and kept at -1.5 kV and the wire is the anode and grounded. When a charged particle cross one tube, leaves a signal; the set of signals in the tubes, reconstructs to a track which represents the path of the crossing object. The space between the straw tubes is filled with material with different refraction index, this causes charged particles crossing it to emit transition radiation thus leading to some straw to have a much stronger signal. The transition radiation depends on the speed of the particles which in turn depends on the initial energy and the mass of the particles thus lighter particles will have higher transition energy and stronger signal in the straw tubes. Tracks with several strong signal straw, can be identified as belonging to electrons (the lightest charged particle).

An additional layer, the Insertable B-Layer (IBL), was recently added in the region between the beam pipe and the inner pixel layer (B-layer). It is designed to increase the tracking robustness by replacing damaged parts of the pixel B-layer and increasing the hit redundancy with the higher luminosity (twice the design luminosity) foreseen for the High Luminosity LHC (HL-LHC) in 2020, moreover, being closer to the beam pipe it increases the impact parameter measurement precision. As part of the installation procedure a smaller beam pipe was installed which will be used also in the HL-LHC phase unless an even smaller radius pipe becomes possible [7].

2.2.3 The Calorimeter

The main purpose of a calorimeter is to measure the energy of electrons, photons and hadrons by mean of materials capable of completely absorb the energy of the incoming particles transforming it in some measurable quantity. Calorimeters can be classified in two categories, *electromagnetic* (EM) and *hadronic* depending on the particle they are designed to detect. The EM calorimeters are mainly used to detect photons and electrons while the task of hadronic calorimeters is to identify hadrons. Both types of calorimeters can be further divided into *sampling calorimeters* and *homogeneous calorimeters*. Sampling calorimeters alternates layers of a dense material used to absorb the energy of incident particles (absorber) and an active material to collect the signal. The interaction between the particles and the absorber produces a shower of secondary particles with progressively degraded energy which is deposited in the active material in form of charge or light that can be converted into energy. Homogeneous calorimeters use only one material that serves both as an absorber and an active material [8].

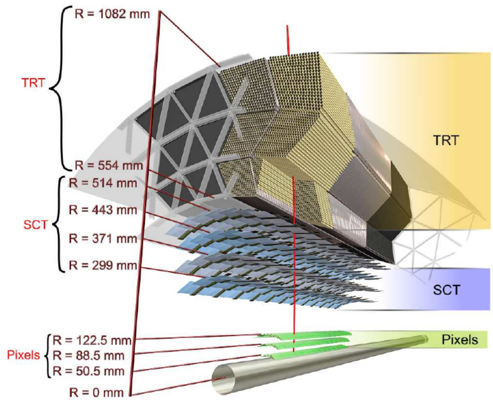

Figure 2.3: Schematic view of a charged track of 10 GeV p_{T} that traverses the different ID sub-detectors. After traversing the beryllium pipe, the track passes through the three cylindrical silicon-pixel layers, the four layers of silicon-microstrip sensors (SCT) and the approximately 36 straws contained in the TRT within their support structure.

The ATLAS calorimeter is a sampling calorimeter covering up the $|\eta| < 4.9$ region the large η coverage, ensures a good missing transverse momentum measurement (see Section 4.2); an illustration of the system is shown in Figure 2.4.

The EM calorimeter has a barrel and two end-caps, covering the $|\eta| < 1.475$ and $1.375 < |\eta| < 3.2$ region respectively. It uses Liquid Argon (LAr) as active material and lead as absorber in an accordion geometry that provides ϕ symmetry without azimuthal cracks. In the region $|\eta| < 1.8$ a presampler consisting of a LAr active region is used to correct for electrons and photons energy loss upstream of the calorimeter.

There are then three hadronic calorimeters: the Tile Calorimeter (TileCal), the Hadronic End-cap Calorimeter (HEC) and the LAr Forward Calorimeter (FCal). The TileCal barrel and extended barrels cover the $|\eta| < 1.0$ and $0.8 < |\eta| < 1.7$ and uses steel as absorber and scintillating tiles connected to photomultipliers tubes through wavelength shifting fibers for readout as an active material. The HEC covers the $1.5 < |\eta| < 3.2$ region and, to avoid drops in material density at the transition, it overlaps slightly with the FCal that covers the $3.1 < |\eta| < 4.9$.

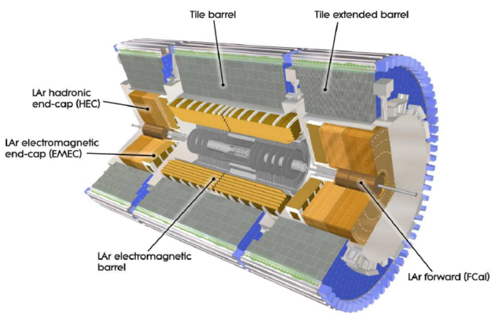

Figure 2.4: Cut-away view of the ATLAS calorimeter system.

2.2.4 The Muon Spectrometer

The Muon Spectrometer (MS) is designed to identify muons and measure their momentum. It is divided in four sub-detectors, the Monitored Drift Tubes (MDT), the Cathode Strip Chambers (CSC), the Resistive Plate Chambers (RPC), and the Thin Gap Chamber (TGC) that. The sub-detectors are immersed in a magnetic field generated by three different toroidal magnets, a barrel toroid covering the $|\eta| < 1.4$ region and two end-caps magnets at $1.6 < |\eta| < 2.7$, which produces a field almost perpendicular to the muon tracks.

The MDT covers the $|\eta| < 2.7$ region and provides a precise measurement of the track coordinates in the principal bending direction of the magnetic field. It uses drift tubes filled with an Ar (93%) and CO_2 (3%) gas mixture and a tungsten-rhenium wire at 3080 V potential as anode. To reconstruct the muon trajectory, the drift time of the ionized charges is used to determine the minimum distance between the wire and the muon. The CSC covers the $2.0 < |\eta| < 2.7$ region and is a multi-wire proportional chamber with cathodes segmented in strips, one perpendicular to the anode wire, providing the precision coordinate, and the other parallel to it (giving the transverse coordinate).

The RPC and the TGC cover the $|\eta| < 1.05$ and $1.05 < |\eta| < 2.7$ regions respectively. They contribute to the Level 1 trigger providing bunch-crossing identification, it allows to select high and low p_{T} tracks and measure the muon coordinate in the direction orthogonal to that determined by MDT and CSC.

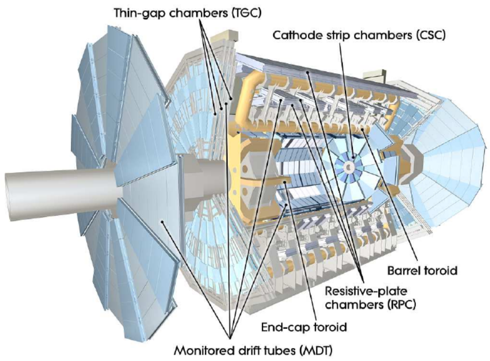

Figure 2.5: Cut-away view of the ATLAS muon spectrometer.

2.2.5 The Forward Detectors

The ATLAS forward region is covered by three smaller detectors: the LUminosity measurement using Cerenkov Integrating Detector (LUCID), the Absolute Luminosity For ATLAS (ALFA) and the Zero-Degree Calorimeter (ZDC). LUCID is located at ± 17 m from the IP, it is designed to monitor the relative luminosity (**relative to what?**) by detecting the inelastic pp scattering. The ZDC is located at ± 140 m from the IP, it consists of alternating layers of quartz rods and tungsten plates designed to measure neutron at $|\eta| < 8.2$, its purpose is to measure the centrality in heavy-ion collisions. ALFA is located at ± 240 m and is designed to measure the absolute luminosity via elastic scattering at small angles.

2.2.6 Track reconstruction

Object reconstruction is the process that associates the signal left in the detector by charged particles to physical objects through a series of algorithms.

Charged particles that moves through a homogeneous solenoidal magnetic field along the z direction, follow helical trajectories. The projection of a helix on the xy plane is a circle and, in order to uniquely parametrize a helix in three dimensions, five parameters are needed. A common choice is to use the *perigee* parameters, where the perigee is the point of closest approach to the beam axis. With this choice, the five parameters are:

- The signed curvature C of the helix, defined as $C = q/2R$ where q is the particle charge and R is the radius of the helix. This is related to the transverse momentum $p_{\mathrm{T}} = qB/C$, where B is the magnetic field measured in Tesla, C is measured in m^{-1} and p_{T} in GeV / c^2.
- The distance of closest approach d_0 in the xy plane.
- The z coordinate of this point, denoted by z_0.
- The azimuthal angle ϕ_0 of the tangent to this point.
- The polar angle θ to the z-axis.

The perigee and the track parameters are schematized in Figure 2.6

try to find what *LooseTrackOnly* is that I mention on subsection 4.1.3

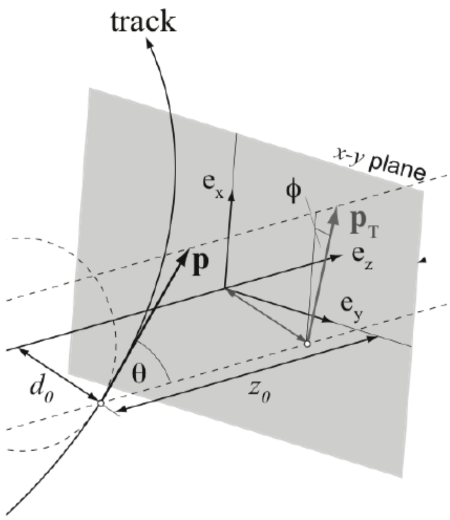

Figure 2.6: Perigee parameters

2.2.7 The Trigger System

The bunch crossing rate at LHC is 40 MHz for a bunch spacing of 25 μs (about 7 meters), in reality there are several bigger gaps bringing this rate down to $\approx$ 31 MHz. Each event recorded by ATLAS require $\approx$ 1.4 MB of disk space, with approximately

20 to 50 collisions per bunch crossing, the storage space required to record all the events would be ≈ 60 TB/s. This is not feasible thus only the most interesting events are selected and stored on disk. The *trigger system* decides whether to keep or not a collision event for later studies, it consists of a hardware based Level One (L1) trigger and a software based High Level Trigger (HLT).

The L1 trigger determines Region of Interest (RoIs) in the detector using custom hardware and coarse information from the calorimeter and the muon system. The L1 trigger is capable of reducing the event rate to 100 kHz with a decision time for a L1 accept of 2.5 μs. The RoIs from the L1 trigger are sent to the HLT where different algorithms are run using the full detector information and reducing the L1 output rate to 1 kHz with a processing time of 200 ms [9]. A schematic overview of the ATLAS trigger and data acquisition system is shown in Figure 2.7.

In this analysis the HLT_xe70 trigger has been used, it receives an L1 accept that selects events with a missing energy (see Section 4.2) greater than 50 GeV, no muons are used in the reconstruction of the missing energy. At the HLT level, events with a missing energy greater than 70 GeV are then selected. (**Are at the HLT level the muon used? Otherwise, what's the point of this cut? Couldn't the event be selected directly using a 70 GeV cut at L1?**)

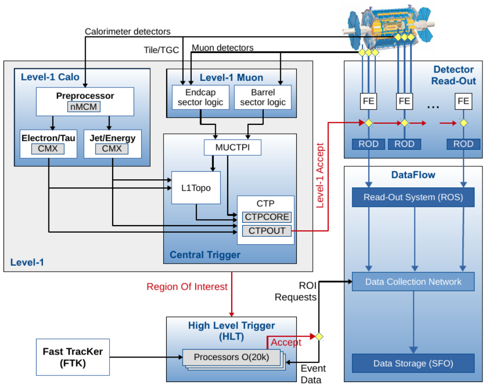

Figure 2.7: Schematic view of the ATLAS trigger and data acquisition system.

Chapter 3

Noise Studies with the Tile Calorimeter

3.1 Calorimetry

The particle interaction with matter causes them to lose energy. The particle's energy and its type determines the processes causing the energy loss; these can be of two kind, *electromagnetic* and *hadronic*. In this section a brief overview of the physics behind the two is given.

3.1.1 The Electromagnetic Shower

Electrons and photons can lose energy by *ionization* or *radiation*. When electrons with energies greater than ~ 10 MeV interacts with the field generated by the absorber layer nuclei, a deceleration and thus a loss of energy in form of a photon (*Bremsstrahlung*) is experienced. Photons in this energy range produce mostly electron-positron pairs. At lower energies, electrons lose their energy through ionization and thermal excitation of the active material atoms while photons lose energy through the Compton scattering and the photoelectric effect.

Electrons and photons with a sufficient amount of energy interacting with an absorber, produce secondary photons through Bremsstrahlung or secondary electrons and positrons by pair production. These secondary particles will produce more particles through the same mechanisms giving rise to a shower of particles with progressively lower energies. This process goes on until the energy of the electrons falls below a critical energy, ϵ, where ionization and excitation becomes the dominant effects [8].

3.1.2 Hadronic Shower

In a similar way to the electromagnetic shower, hadrons lose energy through strong interaction with the calorimeter material. The strong interaction is responsible for the production of energetic secondary hadrons with momenta typically at the GeV scale and nuclear reactions such as excitation or nucleon spallation in which neutrons and protons are released from the nuclei with a characteristic energy at the MeV scale.

The hadron produced are mainly pions, of these, 90% are neutral pions which decay to photons ($\pi \to \gamma\gamma$). The photons produced this way will initiate an electromagnetic shower as described in Section 3.1.1 transferring energy from the hadronic part to the electromagnetic and not contributing any more to hadronic processes. The nucleons released by excitation or nuclear spallation, require an energy equal to their binding energy to be released and are not recorded as a contribution to the calorimeter signal thus producing a form of *invisible energy.* Some detectors can compensate for the loss of invisible energy, these are called *compensated calorimeters* [8].

3.1.3 Energy Resolution

The energy resolution of a detector measure its capability of distinguishing between radiation of similar energies; the better the energy resolution, the better it can separate energy peaks belonging to different decays.

The energy resolution, in general, can be written as:

$$\frac{\sigma_E}{E} = \frac{a}{\sqrt{E}} \oplus \frac{b}{E} \oplus c, \tag{3.1.1}$$

where the $\oplus$ symbol indicates a quadratic sum. The first term in the equation is the *stocastic term*, it is due to fluctuations related to the physical development of the shower. In homogeneous calorimeters, this term is small because the energy deposited in the active volume by a monochromatic beam of particles is constant for each event. In a sampling calorimeter, the active layers are interleaved with absorber layers thus the energy deposited in the active material fluctuates event by event. These are called *sampling fluctuations* and represent the greatest limitation to energy resolution in these kind of calorimeters due to the variation in the number of charged particles which cross the active layers. The second term in eq. (3.1.1) is called the *noise term*, it comes from the electronic noise of the detector readout chain. Sampling or homogeneous calorimeters which collect the signal in the form of light, using for example a photo-multiplier tube with a high gain multiplication of the signal with a low electronic noise, can achieve low levels of noise. Calorimeters that collect the signal in form of charge, must use an pre-amplifier having thus a higher level of noise. In sampling calorimeters, the noise term can be further reduced by increasing the sampling fraction, this way there is a larger signal coming from the active material and a higher noise-to-signal ratio. The last term of the equation is the *constant term*, it does not depend on the energy of the particles but includes all the non uniformities in the detector response such as instrumental effect, radiation damage, detector aging or the detector geometry [8].

3.2 The ATLAS TileCal

I'm not very happy with this section, will have a review! TileCal is the central hadronic calorimeter of the ATLAS experiment, it is designed for energy reconstruction of hadrons, jets, tau particles and missing transverse energy. TileCal is a scintillator steel non compensated sampling calorimeter and it covers the region of $|\eta| < 1.7$. The scintillation light produced in the tiles is transmitted by wavelength shifting fibers to PhotoMultiplier Tubes(PMTs). The analog signals from the PMTs are amplified, shaped and digitized by sampling the signal every 25 ns. The TileCal front end electronics read out the signals produced by about 10000 channels measuring energies ranging from 30 MeV to 2 TeV. The readout system is responsible for reconstructing the data in real time. The digitized signals are reconstructed with the Optimal Filtering algorithm, which computes for each channel the signal amplitude, time and quality factor at the required high rate.

TileCal is designed as one Long Barrel (LB) and two Extended Barrel (EB). The barrels are further divided, according to their geometrical position on the z-axis, in partitions called EBA, LBA, EBC and LBC (see Section 2.2.1). Each partition consists of 64 independent wedges (see Figure 3.1) along the azimuthal direction called *modules*; the LBA and EBA partitions are shown in Figure 3.2.

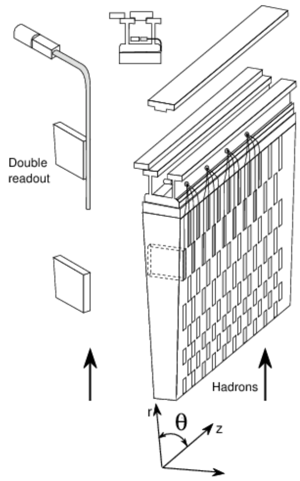

Figure 3.1: Cut away showing the optical read out and design of a TileCal module.

Between the LB and the EB there is a 600 mm gap needed for the ID and the LAr cables, electronics and services. Part of the gap contains the Intermediate Tile Calorimeter (ITC), a detector designed to maximize the active material while leaving enough space for services and cables. The ITC is an extension of the EB and it occupies the $0.8 < |\eta| < 1.6$ region. The combined $0.8 < |\eta| < 1.0$ part is called *plug* and in the $1.0 < |\eta| < 1.6$ region, due to the very limited space, the ITC is composed of only scintillator. The scintillators between $1.0 < |\eta| < 1.2$ are called *gap scintillators*, while those between $1.2 < |\eta| < 1.6$ are called *crack scintillators*. The plug and the gap scintillators mainly provide hadronic shower sampling while the crack scintillator, which extends to the region between the barrel and the end-cap cryostats, samples the electromagnetic shower in a region where the normal sampling is impossible due to the dead material of the cryostat walls and the ID cables.

TileCal is also divided in longitudinal layers, the A, BC and D layers as shown in Figure 3.2; the two innermost layers have a $\Delta\eta \times \Delta\phi$ segmentation of 0.1×0.1 while in the outermost, the segmentation is 0.1×0.2. Each layer is logically divided into *cells* by grouping together in the same PMT the fibers coming from different scintillators belonging to the same radial depth. The gap/crack scintillators are also called E layer cells.

The energy resolution for jets of TileCal is:

$$\frac{\sigma_E}{E} = \frac{50\%}{\sqrt{E}} \oplus 3\% \tag{3.2.1}$$

for $|\eta| < 3$. The 3% constant term becomes dominant for high energy hadrons where an increase in energy resolution is expected [10].

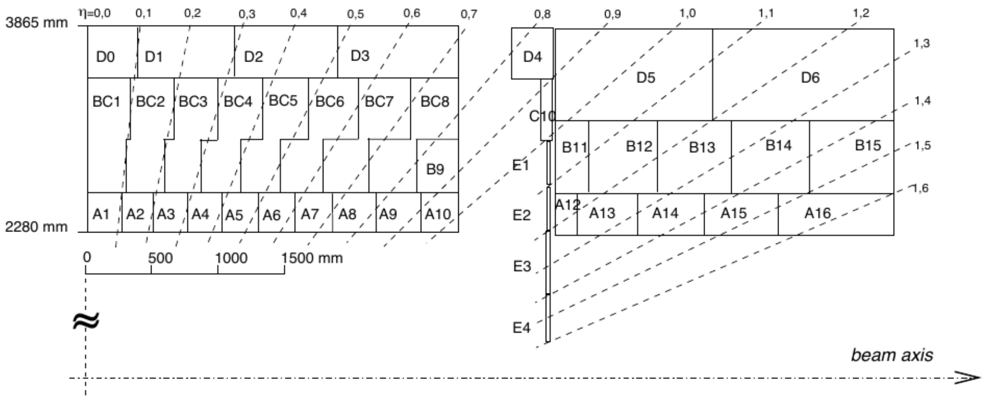

Figure 3.2

3.2.1 Signal Reconstruction

The TileCal cells are read out by two PMTs with the exception of the E layer cells that are connected to only one photomultiplier tube using Wavelength Shifting Fibers (WSF). Each PMT is associated to an electronic read-out channel. The current pulse from the PMTs is shaped and amplified by the 3-in-1 card. There are two possible gains: High Gain (HG) and Low Gain (LG), with an amplification ratio of 64. The 3-in-1 card forms the front-end electronics of the read-out chain and provides three basic functions: shaping of the pulse, charge injection calibration and slow integration of the PMT signals for monitoring and calibration [10] (**don't really know much about this**). Up to twelve 3-in-1 cards are serviced by a motherboard that provides power and individual control signals. The amplified signal is sent to two Analog to Digital Converters(ADCs) synchronous with the 40 MHz LHC clock thus sampling the signal every 25 ns. For optimization and efficiency reasons, 7 samples for each pulse are taken and sent to the ReadOut Drivers(RODs) for a L1 accept.

Optimal Filtering

The seven samples are used to reconstruct the amplitude of the pulse using the Optimal Filtering (OF) method. The estimate of the amplitude is given by:

$$\hat{A} = \sum_{i=0}^{N} a_i S_i \tag{3.2.2}$$

where S_i are the digitized samples, N is the number of samples and a_i are computed weights that minimize the effect of the electronic noise on the amplitude reconstruction. The procedure minimizes the variance of the amplitude distribution. In order to make the amplitude reconstruction independent from phase and signal baseline due to electronic noise (*pedestal*), the following constraints are used:

$$\sum_{i=0}^{N} g_i a_i = 0 \tag{3.2.3}$$

$$\sum_{i=0}^{N} g_i' a_i = 0 \tag{3.2.4}$$

$$\sum_{i=0}^{N} a_i = 0 \tag{3.2.5}$$

where g_i and g_i' are the pulse shape function from the shaper and its derivative [11].

The TileCal Calibration

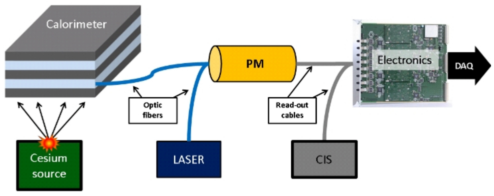

Figure 3.3: The ATLAS TileCal calibration chain.

The energy deposited in the calorimeter cell is proportional to the reconstructed amplitude. The amplitude is originally measured in ADC counts and needs to be converted in GeV for physics analysis using the formula:

$$E[GeV] = \hat{A}[ADC] \times C_{ADC\to pC} \times C_{\text{laser}} \times C_{Cs} \times C_{pC\to GeV} \tag{3.2.6}$$

where $\hat{A}[ADC]$ is the amplitude estimate in ADC counts, $C_{ADC\to pC}$ is determined using the Charge Injection System (CIS), $C_{pC\to GeV}$ is measured during testbeam using electrons with a well defined energy and converts the deposited charge to energy in GeV, the laser system allows to determine the value of the C_{laser} constant while the Cesium sets the C_{Cs} factor.

The CIS calibrates the read out electronics by injecting a known charge and measuring the resulting response of the electronics. The *laser* system main purpose is to monitor the photomultipliers tubes and the downstream electronics. Well calibrated light pulses are sent to the PMTs and by reconstructing the signal it is possible to extract the PMTs' gain. The *cesium* system, circulate a Cs source through each scintillating tile using an hydraulic system, the PMTs signal is continuously read out through an integrator. This system allows to adjust the EM scale and equalize the calorimeter cell response.

3.2.2 Electronic Noise

TileCal periodically performs sets of recorded event (*runs*) with no signal in the PMTs, called *pedestal runs*; during these runs, each channel is read out using both, HG and LG for about 100000 events. These events are sampled every 25 ns in 7 samples as in normal physic runs and are normally distributes around a mean value called *pedestal*. The Root Mean Square (RMS) of the pedestal is defined as *noise*. Pedestal runs are used to calculate different parameters that allow to describe the electronic noise called *noise constants*. Two different sets of noise constants are computed: *Digital Noise* (or *Sample Noise*) and *Cell Noise*.

Digital Noise

The digital noise is measured in ADC counts for each PMT in both gains, HG and LG. The noise constants together with all detector conditions are stored in the ATLAS Condition Database (COOL). These constants are the RMS of the seven samples within each event, also called High Frequency Noise (HFN) and the RMS of the first digitized sample in each event or Low Frequency Noise (LFN). The digital noise is used for monitoring and for Monte Carlo (MC) noise simulation.

Cell Noise

In most cases, cell noise is the combination of the pulse from the PMTs connected to a cell (as mentioned the E layer cells are connected to only one PMT). The digital noise from the PMTs is added quadratically and converted in MeV using the calibration constants, this results in four gain combinations: High Gain – High Gain (HGHG), Low Gain – Low Gain (LGLG), Low Gain – High Gain (LGHG) and Hig Gain – Low Gain (HGLG).

The cell noise is used in the baseline algorithm, the *topological clustering* algorithm [12], for the identification of the energy deposits. The algorithm assumes that the noise in all the calorimeter cells is normally distributed with significance (the ratio between the deposited energy and the parameter σ used to describe the cell noise) expressed in units of Gaussian sigmas. In the algorithm, cluster of cells called *topoclusters*, are formed by testing the energy deposit in a cell for a significant incompatibility with a noise only hypothesis. The algorithm starts by finding the *seed cells* with $E > 4\sigma$ where σ is the measured RMS of the energy distribution for every cell in the pedestal run. The second step is to add to the seeds neighbor cells that satisfy the $E > 2\sigma$ condition. Finally an additional layer of cells with $E > 0$ is added to the perimeter of the cluster before applying the splitting algorithm to separate the topoclusters based on the local energy maxima.

Figure 3.4 shows a comparison between the cell noise and the fitted σ parameter of a normal distribution. The ratio RMS / $\sigma = 1$ indicates a perfect agreement between the measured and the fitted amplitude distribution for a single Gaussian hypothesis; as can be seen, with an old model of Low Voltage Power Supply (LVPS) (blue square) the ratio RMS / σ can be larger thus worsening the performance of the topological clustering algorithm. For this reason a double Gaussian distribution is used to fit the energy distribution, the probability density function is defined as:

$$f_{2g} = \frac{1}{1+R}\left(\frac{1}{\sqrt{2\pi}\sigma_1}e^{-\frac{x^2}{2\sigma_1^2}} + \frac{R}{\sqrt{2\pi}\sigma_2}e^{-\frac{x^2}{2\sigma_2^2}}\right) \tag{3.2.7}$$

where R is the relative normalization of the two Gaussians and σ_1, σ_2 and R are independent parameters. These three are used to define the region $\sigma_{\text{eff}}(E)$ where the significance for the double Gaussian is the same as the one σ region for a single Gaussian, i.e. $\int_{-\sigma_{\text{eff}}}^{\sigma_{\text{eff}}} f_{2g} = 0.68$ [13]. In terms of σ_{eff}, for an energy deposit E, the significance can be expressed as:

$$\frac{E}{\sigma_{\text{eff}}(E)} = \sqrt{2}\ \text{Erf}^{-1}\left(\frac{\sigma_1 \text{Erf}\left(\frac{E}{\sqrt{2}\sigma_1}\right) + R\sigma_2 \text{Erf}\left(\frac{E}{\sqrt{2}\sigma_2}\right)}{\sigma_1 + R\sigma_2}\right) \tag{3.2.8}$$

where Erf is the error function. Eq. (3.2.8) is the input to the clustering algorithm, moreover this definition allows to use the same unit to describe the noise for both the

TileCal and LAr calorimeters. The region $\sigma_{\text{eff}}(E)$ is commonly referred to as *cell noise* and together with the three double Gaussian parameters (σ_1, σ_2 and R) is stored in the COOL database.

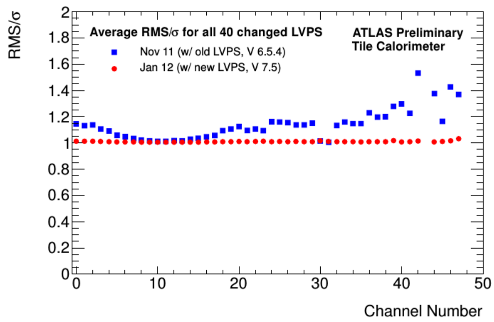

Figure 3.4: Comparison between the TileCal electronic noise, measured as the RMS of the reconstructed amplitude distribution in pedestal runs and the σ of the Gaussian fit of the distribution for the old and new LVPS.

3.3 The 2011 ATLAS Run I Reprocessing

As new information about the detector becomes available, an update of the calibration constants and thus of the reconstructed energy might take place; this procedure is called *reprocessing*.

3.3.1 Perfromance

Insert this part

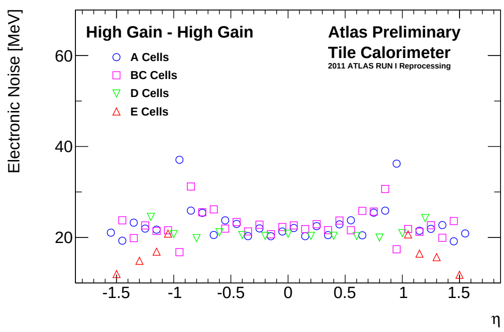

Figure 3.5

3.3.2 Validity Checks

A certain set of calibration constants is valid over a period of time called Interval Of Validity (IOV). The cell noise can vary due to a change in the calibration, the digital noise or the channel status in a particular run. This change must be consistent and checked.

The different TileCal subsystems (laser, CIS, etc.) all use a common software framework, TileCal Universal Calibration Software (TUCS), to perform validity checks on a number of different studies. To test the stability over time of the updated noise constants, a set of python scripts was developed to expand the TUCS functionality. These scripts allow to visually display the relative change of the cell noise and digital noise constants, the channel status and the ratio between the cell noise and a variable called $\mathrm{RMS_{eff}}$ and defined as:

$$\mathrm{RMS_{eff}} = \sqrt{(1-R)\sigma_1^2 + R\sigma_2^2} \tag{3.3.1}$$

where σ_1, σ_2 and R are the free parameter in the double Gaussian model (see Section 3.2.2). The ratio σ / $\mathrm{RMS_{eff}}$, where σ is the cell noise, can be used to test the goodness of the double Gaussian model: if σ / $\mathrm{RMS_{eff}}$ equals one, the double Gaussian well models the noise, if it is larger, it means that there is noise that is not well described by it.

Figure 3.6 shows the time evolution plot for two representative TileCal cells. In Figure 3.6a it can be seen that cell number 2 in the BC layer (BC2) of the 41st module in the C side of LB (LBC 41) is stable over several pedestal runs. In Figure 3.6b on the other hand, it is possible to see a variation in the cell noise and, accordingly, of the σ / $\mathrm{RMS_{eff}}$ without a compatible variation in the calibration, in the digital noise constants or in the channel status. The term *jump* will be used in the following to indicate a variation in the cell noise not compatible with a change in the other quantities.

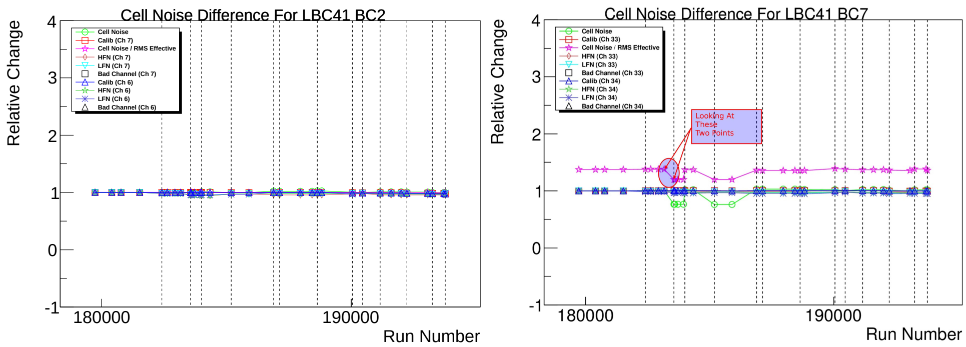

(a) (b)

Figure 3.6: Time evolution plots for two different representative cells in the calorimeter. The plot shows the change relative to the first run considered of several quantities for different IOVs (vertical dashed lines).

This problem was investigated by writing a software to manually fit the pulse shape and calculate the noise constants focusing on two specific IOVs, $[183110, 183382[$ and $[183382, 183515[$. Some calorimeter cells without jump were used to validate the noise constants calculated with the fit and those stored in the COOL database. Figure 3.7 shows the control cell energy distribution with the double Gaussian fit superimposed for two runs where the jump was present in other cells. The results for the ratio of the amplitude of the double Gaussian model (R), the $\mathrm{RMS_{eff}}$ and the σ / $\mathrm{RMS_{eff}}$ obtained with the fit are:

$$\begin{cases} R : 0.0003 \\ \mathrm{RMS_{eff}} : 20.12 \\ \sigma/\mathrm{RMS_{eff}} : 0.998 \end{cases} \rightarrow \begin{cases} R : 0.0002 \\ \mathrm{RMS_{eff}} : 20.07 \\ \sigma/\mathrm{RMS_{eff}} : 0.995. \end{cases} \tag{3.3.2}$$

They are in good agreement with the values stored in the COOL database and reported in Table 3.1.

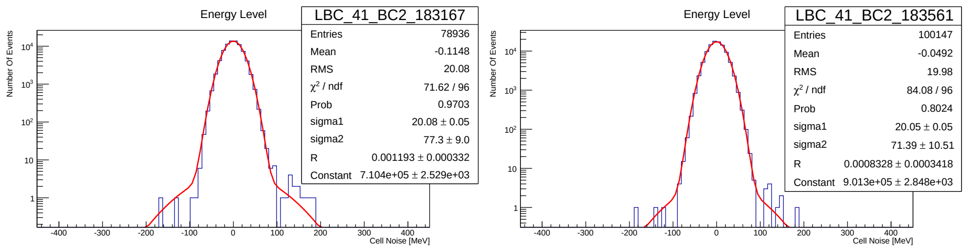

(a) Fit before jump. (b) Fit after jump.

Figure 3.7: Fit of the reconstructed pulse shape on a control cell with no variation (jump) in the cell noise.

LBC41 BC2 Values From Database	
Before Jump	
σ:	20.08
σ_1:	19.97
σ_2:	80.59
R:	0.00026
$\mathrm{RMS_{eff}}$:	20.01
σ / $\mathrm{RMS_{eff}}$:	1.0035

LBC41 BC2 Values From Database	
After Jump	
σ:	19.98
σ_1:	19.94
σ_2:	71.41
R:	0.00023
$\mathrm{RMS_{eff}}$:	19.97
σ / $\mathrm{RMS_{eff}}$:	1.0006

Table 3.1: The table reports the cell noise constants stored in the COOL database for two different run numbers corresponding to before and after the jump for a cell where there is no variation in the cell noise.

Figure 3.8 shows the energy distribution with the double Gaussian fit superimposed on the seventh cell of the BC layer (BC7) on the C side of the LB partition of the 41st module (LBC 41). The cell had the jump under investigation (see Figure 3.6) and this is reflected in the fit results:

$$\begin{cases} R : 0.042 \\ \mathrm{RMS_{eff}} : 29.59 \\ \sigma/\mathrm{RMS_{eff}} : 1.37 \end{cases} \rightarrow \begin{cases} R : 0.014 \\ \mathrm{RMS_{eff}} : 26.67 \\ \sigma/\mathrm{RMS_{eff}} : 1.2. \end{cases} \tag{3.3.3}$$

Also in this case, the noise constants from the fit, are in agreement with those stored in the COOL database and reported in Table 3.2. Moreover, the χ^2 of the distribution and the ration σ / $\mathrm{RMS_{eff}}$ greater than one, imply that the double Gaussian model is not a good model in this case.

After consultation with experts [14], it was suggested that this behavior could be caused by the Tile Noise Filter (TNF). Many electronic devices are involved in the signal reconstruction, the noise of these can be altered in a coherent way (by electromagnetic field emission for instance) and thus altering the jet and missing transverse energy reconstruction. This alteration is called *coherent noise* and what the TNF does is to subtract it from the channels connected to the same motherboard (see Section 3.2.1) on an event-by-event basis. The cell noise war recalculated without without

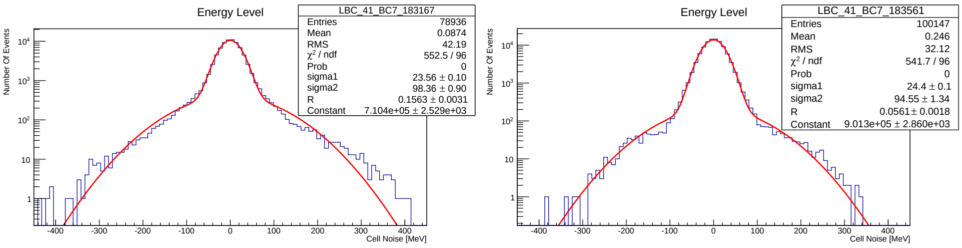

(a) Before jump.

(b) After jump.

Figure 3.8: Fit of the reconstructed pulse shape on a cell with variation (jump) in the cell noise non compatible with a change in the calibration, digital noise or channel status.

LBC41 BC7 Values From Database	
Before Jump	
σ:	42.19
σ_1:	24.26
σ_2:	99.16
R:	0.037
RMS_{eff}:	30.56
σ / RMS_{eff}:	1.38

LBC41 BC7 Values From Database	
After Jump	
σ:	32.12
σ_1:	24.42
σ_2:	94.56
R:	0.014
RMS_{eff}:	26.79
σ / RMS_{eff}:	1.20

Table 3.2: The table reports the cell noise constants stored in the COOL database for two different run numbers corresponding to before and after the jump for a cell where there is a variation in the cell noise was spotted.

noise filter and the corresponding distribution re-fitted obtaining:

$$\begin{cases} R : 0.0750867 \\ \text{RMS}_{\text{eff}} : 47.49 \\ \sigma/\text{RMS}_{\text{eff}} : 1.49 \end{cases} \rightarrow \begin{cases} R : 0.075 \\ \text{RMS}_{\text{eff}} : 48.91 \\ \sigma/\text{RMS}_{\text{eff}} : 1.44. \end{cases} \tag{3.3.4}$$

Comparing Equation 3.3.4 with Equation 3.3.3 it is possible to see that without TNF, there is no jump.

Chapter 4

Physical Objects Reconstruction

4.1 Lepton Reconstruction and Identification

This analysis uses electrons, muons, jets and missing transverse momentum ($E_{\mathrm{T}}^{\mathrm{miss}}$). Two types of electrons, muons and jets are also defined: *baseline* and *good*, where the former one is used for overlap removal and preselection while the latter for selecting the objects used to define the signal and control regions. In the following a brief introduction to the identification criteria of these objects is presented.

4.1.1 Primary Vertex

In *pp* collisions with high luminosity, multiple interactions occur on a given bunch crossing, the space location of the collision is called *vertex* and the the hard scatter vertex (the one that has the highest $\sum p_{\mathrm{T}}^2$ of constituent tracks) that triggered the recording of the event is called Primary Vertex (PV), the rest are called *pile-up vertices*. The reconstruction of the PV generally happens in two stages that are often not distinguishable from each other. The *vertex finding* associates reconstructed tracks to a particular vertex candidate and the *vertex fitting* reconstructs the actual vertex position, refits the incident tracks and estimates the quality of the fit [15].

In the current analysis events are required to have at least one PV with two associated tracks.

4.1.2 Overlap Removal

During object reconstruction, it may happen that different algorithms identify the same track and cluster as different particles, this results in a duplicate object. In physics analyses a decision must be made on which interpretation to give to the reconstructed object, this process is called Overlap Removal (OR) [16].

In this analysis, an overlap removal is applied to electrons, muons and jets that pass the baseline criteria and the following objects are removed:

- Remove jet in case any pair of jet and electron satisfies $\Delta R(j, e) < 0.2$.
- Remove electron in case any pair of jet and electron satisfies $0.2 < \Delta R(j, e) < 0.4$.

- Remove muon in case any pair of muon and jet with at least 3 tracks satisfies $\Delta R(j, \mu) < 0.4$.
- Remove jet if any pair of muon and jet with less than 3 tracks satisfies $\Delta R(j, \mu) < 0.4$.

4.1.3 Electrons

Electrons are identified in the central part of the ATLAS detector ($|\eta| < 2.47$) by an energy deposit in the electromagnetic calorimeter and an associated track in the inner detector. Signal electrons are defined as prompt electrons coming from the decay of a W, Z boson or a top quark while background electrons come from hadronic jets, photon conversion and semi-leptonic heavy flavor hadron decay. A likelihood discriminator is formed using the shower shape in the EM calorimeter, the track-cluster matching, some of the track quality distributions from signal and background simulation and cuts on the number of hits in the ID. Cuts that depends on $|\eta|$ and E_{T} on the likelihood estimator allow to distinguish between signal and background electrons.

Electron identification efficiencies are measured in pp collisions data and compared to efficiencies measured in $Z \to ee$ simulations. Signal electrons can furthermore be selected with different sets of cuts for the likelihood-based criteria with $\sim 95\%, \sim 90\%$ and $\sim 80\%$ efficiency for electrons with $p_{\mathrm{T}} \sim 40$ GeV. The different criteria are referred to as *loose*, *medium* and *tight* operating points respectively [17] where, for example, a tight criterion lead to a higher purity of signal electrons.

In this analysis, the *baseline electrons* are selected requiring a transverse energy $E_{\mathrm{T}} > 20$ GeV, $|\eta| < 2.47$, they need to satisfy the *loose* likelihood selection criteria, it is required that no dead EM calorimeter Front–End Board (FEB) or High Voltage (HV) channels in the calorimeter cluster are present and that the baseline electron passes the OR. The baseline electron criteria is used to veto electrons used in the muon control regions and the signal region definition. In addition to all the baseline criteria, the *good electron* definition requires the electrons to satisfy the *tight* likelihood selection criteria, the electron track $d_0/\sigma_{d0} < 5$ mm and $|z_0| < 0.5$ mm and the *LooseTrackOnly* electron isolation criteria.

Electron Definition	
Baseline electron	**Good electron**
$E_{\mathrm{T}} > 20$ GeV	*baseline*
$\lvert\eta\rvert < 2.47$	*tight*
loose	$d_0/\sigma_{d0} < 5$ mm
No dead FEB in the EM calo cluster	$\lvert z_0\rvert < 0.5$ mm
No dead HV in the EM calo cluster	*LooseTrackOnly*
passes the OR	

Table 4.1: Monojet electron definition

4.1.4 Muons

Muons are reconstructed using different criteria from the information provided by the ID and the MS leading to four different types of muons. The Stand Alone (SA) muons use only the MS information to reconstruct the muon's trajectory; the Combined (CB), where the track is independently reconstructed in the ID and the MS and then combined; the Segment Tagged (ST) are identified as muons only if the track in the ID is, after being extrapolated to the MS, associated to at least one local track segment in the MDT or CSC chambers and finally the Calorimeter Tagged (CT) where tracks in the ID are associated to an energy deposit in the calorimeter compatible with a minimum ionizing particle. CB candidates perform best in terms of muon purity and momentum resolution.

Muons are identified using quality requirements specific to each of the four type of muons aiming at rejecting muons coming from pion and kaon decays and guarantee a robust momentum measurement. The *loose* identification criteria maximize the reconstruction efficiency and provide good muon tracks; the *medium* criteria minimize the systematic uncertainties associated to muon reconstruction and calibration; the *tight* muons optimize the purity of the sample and the *high* p_{T} maximize the momentum resolution for tracks with transverse momenta above 100 GeV[18].

This analysis uses the CB muons that pass the medium identification criteria, moreover the *baseline muons* are required to have $p_{\mathrm{T}} > 10$ GeV and $|\eta| < 2.5$, they are used in the OR, the $E_{\mathrm{T}}^{\mathrm{miss}}$ definition and in the lepton veto used to define the signal and control regions. The *good muons* are required to pass the baseline selection criteria, moreover $d_0/\sigma_{d0} < 3$ mm, $|z_0 \sin\theta| < 0.5$ mm. The good muons are used in the one muon and di-muon control regions.

Muon Definition	
Baseline muon	**Good muon**
CB muon	*baseline*
Medium id. criteria	$d_0/\sigma_{d0} < 3$ mm
$p_{\mathrm{T}} > 10$ GeV	$\lvert z_0 \sin\theta\rvert < 0.5$ mm
$\lvert\eta\rvert < 2.5$	

Table 4.2: Monojet muon definition

4.2 Missing Transverse Energy

Due to the energy conservation and the fact that the proton bunches are parallel to the z-axis, the momentum of the collision products in the transverse plane should sum to zero. Any energy imbalance is known as *missing transverse momentum* ($E_{\mathrm{T}}^{\mathrm{miss}}$), it may indicate weakly interacting stable particles (neutrinos within the SM, new particles in beyond SM models) or non reconstructed physical objects that escape the detector acceptance. Physical objects that are fully reconstructed and calibrated such as electrons, photons, hadronically decaying tau-leptons, jets or muons are called *hard objects* and are used to compute the missing transverse momentum in an event [19]. The x and y components of the $E_{\mathrm{T}}^{\mathrm{miss}}$ can be written as:

$$E_{\mathrm{x(y)}}^{\mathrm{miss}} = E_{\mathrm{x(y)}}^{\mathrm{miss,\,e}} + E_{\mathrm{x(y)}}^{\mathrm{miss},\,\gamma} + E_{\mathrm{x(y)}}^{\mathrm{miss},\,\tau} + E_{\mathrm{x(y)}}^{\mathrm{miss,\,jets}} + E_{\mathrm{x(y)}}^{\mathrm{miss},\,\mu} + E_{\mathrm{x(y)}}^{\mathrm{miss,\,soft}} \tag{4.2.1}$$

where the terms for jets, charged leptons and photons are the negative sum of the momenta of the respective calibrated object while the *soft term* is reconstructed from the transverse momentum deposited in the detector that is not already associated to hard objects. It may be reconstructed by means of calorimeter-based methods, the so called Calorimeter Soft Term (CST), or using track-based methods known as Track Soft Term (TST).

The CST is reconstructed using energy deposits in the calorimeters which are not associated to hard objects, it arise from soft radiation accompanying the hard scatter event and from underlying event activity (**what is the event activity?**). The *event activity* is estimated using the quantity $\sum E_{\mathrm{T}}$, which is defined as the scalar sum of the transverse momenta of the hard objects and soft term contributions:

$$\sum E_{\mathrm{T}} = \sum p_{\mathrm{T}}^{e} + \sum p_{\mathrm{T}}^{\gamma} + \sum p_{\mathrm{T}}^{\tau} + \sum p_{\mathrm{T}}^{\mathrm{jets}} + \sum p_{\mathrm{T}}^{\mu} + \sum p_{\mathrm{T}}^{\mathrm{soft}}. \tag{4.2.2}$$

A downside of the CST is its vulnerability to pile up.

The TST is built from tracks not associated to any hard object, tracks can be associated to vertices and thus to a particular *pp* collision, making this method robust against pile-up. This method is, however, insensitive to soft terms coming from neutral particles that do not leave a track in the ID, thus the TST $E_{\mathrm{T}}^{\mathrm{miss}}$ is combined with calorimeter-based measurements for hard objects.

Due to its stability against pile-up, this analysis uses the TST $E_{\mathrm{T}}^{\mathrm{miss}}$ term, moreover, the muons are treated as invisible particles in the $E_{\mathrm{T}}^{\mathrm{miss}}$ reconstruction (i.e. $E_{\mathrm{x(y)}}^{\mathrm{miss},\,\mu} = 0$).

4.3 Jets

The color-carrying quarks and gluons, created in the scattering process, undergo the hadronization process which produces collimated bunches of colorless hadrons (jets) which keep track of the energy and the direction of the originating parton. Jets in ATLAS are reconstructed as massless particles using the *anti–k_{t}* algorithm, calibrated and corrected for pile-up contamination. These steps are briefly outlined in the next sections.

4.3.1 The *anti–k_{t}* Algorithm

The anti–k$_{\mathrm{t}}$ algorithm is a sequential recombination algorithm. It defines a distance d_{ij} between the physical objects i and j as:

$$d_{ij} = \min(k_{ti}^{-2}, k_{tj}^{-2})\frac{\Delta_{ij}^2}{R^2} \tag{4.3.1}$$

where $\Delta_{ij}^2 = (\eta_i - \eta_j)^2 + (\phi_i^2 - \phi_j^2)$ and η_i is the rapidity, ϕ_i is the azimuthal angle, k_{ti} is the transverse momentum of the object i and R is the radius parameter that controls the size of the jet and a distance d_{iB} between the object i and the beam (B) defined as:

$$d_{iB} = k_{ti}^{-2}. \tag{4.3.2}$$

This distance is meant to distinguish between hard and soft terms. The algorithm identifies the smallest of the two distances and, if it is d_{ij}, it recombines the i and j objects while if it is d_{iB}, it calls i a jet and removes it from the list of entities. The distances are recalculated and the procedure reiterated until there are no more objects [20].

4.3.2 The Jet Vertex Tagger

The excess transverse energy coming from pile-up jets is generally subtracted on average from the signal energy, however, due to localized fluctuations in the pile-up, some of it remains in the p_{T} of the reconstructed jet. The Jet Vertex Fraction (JVF) is a variable that uses information from the track associated to each jet to identify the origin vertex of each jet and reject it if not coming from a hard-scatter vertex [21]. The JVF can be regarded as a measure of the fraction of the jet energy associated with a primary vertex and is defined as:

$$\mathrm{JVF} = \frac{\sum_k p_{\mathrm{T}}^{\mathrm{trk_k}}(\mathrm{PV_0})}{\sum_l p_{\mathrm{T}}^{\mathrm{trk_l}}(\mathrm{PV_0}) + \sum_{n\geq l}\sum_k p_{\mathrm{T}}^{\mathrm{trk_l}}(\mathrm{PV_n})} \tag{4.3.3}$$

where $\mathrm{PV_0}$ is the primary vertex and $\mathrm{PV_n}$ with $\mathrm{n} \geq 1$ is any other pile-up PV in the same bunch crossing.

Since the JVF denominator increases with the number of reconstructed PV, this introduces a pile-up dependence on the number of PV when minimal JVF criterion are imposed in rejecting pile-up jets. To address this problem, two new variables to separate from Hard Scatter (HS) and Pile Up (PU) jets are introduced: corrJVF and $\mathrm{R_{pT}}$. The former is defined as:

$$\mathrm{corrJVF} = \frac{p_{\mathrm{T}}^{\mathrm{HS}}}{p_{\mathrm{T}}^{\mathrm{HS}} + p_{\mathrm{T}}^{\mathrm{PU,corr}}} \tag{4.3.4}$$

where $p_{\mathrm{T}}^{\mathrm{HS}} = \sum_k p_{\mathrm{T}}^{\mathrm{trk_k}}(\mathrm{PV_0})$ is the scalar sum of the p_{T} of the tracks associated with the jet that comes from the HS vertex and $p_{\mathrm{T}}^{\mathrm{PU,corr}} = \sum_{n\geq l}\sum_k p_{\mathrm{T}}^{\mathrm{trk_l}}(\mathrm{PV_n})/(kn_{\mathrm{trk}}^{\mathrm{PU}})$ is the scalar sum of the associated tracks originating from a pile-up vertex. Since the average $p_{\mathrm{T}}^{\mathrm{PU}}$ increases linearly with the number of pile-up tracks, $n_{\mathrm{trk}}^{\mathrm{PU}}$, $p_{\mathrm{T}}^{\mathrm{PU}}$ is divided by $(kn_{\mathrm{trk}}^{\mathrm{PU}})$ where $k = 0.01$ is the slope of the $\langle p_{\mathrm{T}}^{\mathrm{PU}}\rangle$ dependence with $n_{\mathrm{trk}}^{\mathrm{PU}}$ [22]. The corrJVF corrects the $\mathrm{N_{PV}}$ dependence in the JVF denominator.

The $\mathrm{R_{pT}}$ is defined as:

$$\mathrm{R_{pT}} = \frac{\sum_k p_{\mathrm{T}}^{\mathrm{trk_k}}(\mathrm{PV_0})}{p_{\mathrm{T}}^{\mathrm{jet}}} \tag{4.3.5}$$

where $p_{\mathrm{T}}^{\mathrm{jet}}$ is the fully calibrated jet p_{T}. This variable is defined using tracks associated with the HS vertex, it is at first order independent on the $\mathrm{N_{PV}}$ [23].

The Jet Vertex Tagger (JVT) is constructed from the corrJVF and $\mathrm{R_{pT}}$ by forming a two dimensional likelihood based on the k-nearest neighbor algorithm. Using the JVT algorithm, the HS jet efficiency is stable within 1% up to 35 interactions per bunch crossing [22].

4.3.3 Jet Calibration

The energy distribution inside a jet contains information on the initiating particle. The decay products of very energetic heavy particles, may be all contained in one large radius jet, in this scenario, the invariant mass of the four vector sum of the jet constituents, called the *jet mass*, should peak around the mass m of the heavy particle as long as the jet radius is larger than $2m/p_{\mathrm{T}}$, where p_{T} is the transverse momentum of the initiating particle [24]. The Jet Energy Scale (JES) relates the energy measured by the ATLAS detector to the kinematic properties of the corresponding stable particles, this calibration must take into account the detector effects such as the non compensating nature of the ATLAS hadronic calorimeter (see Section 3.1.2), energy loss due to inactive regions in the detector or particle showers not fully contained in the calorimeter. The energy deposited by electromagnetic showers, known as the *electromagnetic scale*, is the baseline energy scale of the calorimeter and is established during test beam measurements with electrons. The basic jet calibration scheme, applies JES correction to the EM scale and is usually referred to as EM+JES. The Local Cluster Weighting (LCW) is another calibration method that clusters topologically connected cells, classifying them as electromagnetic or hadronic and deriving the energy corrections from single pion MC simulation and dedicated studies to account for the detector effects, the jets calibrated with this method are referred to as LCW+JES. The Global Cell Weighting (GCW) calibration uses the fact that electromagnetic and hadronic showers leave a different energy deposition in the calorimeter cells, with the electromagnetic shower more compact than the hadronic one. The energy correction are then derived for each calorimeter cell within the jet and minimizing the energy resolution. The Global Sequential (GS) method starts from EM+JES calibrated jets and corrects for the fluctuation in particle content of the hadronic shower using the topology of the energy deposits. The corrections are applied in a way that leaves unchanged the mean jet energy [25].

4.3.4 Jet Selection

In order to distinguish jets coming from *pp* collisions from those from a non-collision origin, two jet selection criteria, *loose* and *tight*, are available. The loose selection criteria, provides an efficiency for selecting jets coming from *pp* collisions above 99.5% for $p_{\mathrm{T}} > 20$ GeV, the tight criteria can reject even further background jets [26].

In this analysis the jets are reconstructed using the anti–$\mathrm{k_t}$ algorithm with the radius parameter R = 0.4. The *baseline jets* are required to have $|\eta| < 2.8$ and to make sure they come from a HS vertex, they need to satisfy any of the following:

– the $p_{\mathrm{T}} > 50$ GeV;

– they have $20 < p_{\mathrm{T}} < 50$ GeV and $|\eta| > 2.4$;

– they have $20 < p_{\mathrm{T}} < 50$ GeV, $|\eta| < 2.4$ and JVT > 0.64.

Furthermore, events in which the jets, after the OR is applied, fail the loose selection criteria are disregarded. Finally the most energetic jet in the event (the *leading jet*) is required to pass the tight selection criteria. The *good jets* require an increased p_{T} threshold of 30 GeV and at most 4 HS jet in the event.

Jet Definition	
Baseline jet	**Good jet**
R = 0.4 $\lvert\eta\rvert < 2.8$ *Loose* selection criteria *Tight* on the leading jet any of: • $p_{\mathrm{T}} > 50$ GeV • $20 < p_{\mathrm{T}} < 50$ GeV, $\lvert\eta\rvert > 2.4$ • $20 < p_{\mathrm{T}} < 50$ GeV, $\lvert\eta\rvert < 2.4$, JVT > 0.64	*baseline* at most 4 jets $p_{\mathrm{T}} > 30$ GeV

Table 4.3: Monojet jet definition

Chapter 5

The Monojet Signature

5.1 Motivation

Events with an energetic jet p_{T} and large $E_{\mathrm{T}}^{\mathrm{miss}}$ in the final state, constitute a clean signature for new physics searches at hadron colliders. Signals that can be studied with this experimental signature include the production of WIMPS, the ADD model for large extra dimensions and SUSY.

Fix this part

If the mass difference between the sparticles is small, the sensitivity to new physics signal of many standard SUSY searches is reduced due to the low amount of missing energy and the corresponding low transverse momentum of the associated jets. (why is that so? Try to think and find out) If the event has an ISR, the amount of missing energy and the corresponding transverse momentum jets will be large leading thus to a clean signature for the monojet

It is possible to estimate, from eq. (1.4.2), the scale at which new physics is expected. Using $m_H = 125$ GeV [27], we get that $\Lambda \approx 1$ TeV; thus, if the naturalness criterion holds, we expect the two main experiments at LHC, ATLAS and CMS, to find signal for new physics at the TeV scale.

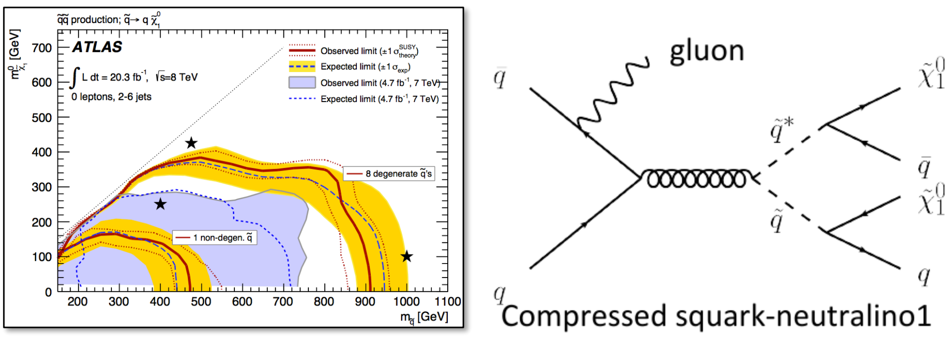

(a) (b)

Figure 5.1

5.2 Event Selection

The search is carried out in *pp* collisions using the data collected by the ATLAS experiment during the 2015 Run II corresponding to a total integrated luminosity of 3.2 fb^{-1}.

Chapter 6

Conclusions

Bollocks! We are 95% confident that we didn't see a thing! . . .

Appendix A

Some title

Acronyms

E_{T} *transverse energy*. 13

η *pseudorapidity*. 13

$E_{\mathrm{T}}^{\mathrm{miss}}$ *missing transverse momentum*. 29

p_{T} *transverse momentum*. 13

pp proton-proton. 11

ADC Analog to Digital Converter. 22

ALFA Absolute Luminosity For ATLAS. 16

ATLAS A Toroidal LHC apparatuS. 12

CB Combined. 29

CERN European Organization for Nuclear Research. 11

CIS Charge Injection System. 23

CSC Cathode Strip Chambers. 16

CST Calorimeter Soft Term. 29

CT Calorimeter Tagged. 29

EB Extended Barrel. 21

EM *electromagnetic*. 14

FCal LAr Forward Calorimeter. 15

HEC Hadronic End-cap Calorimeter. 15

HFN High Frequency Noise. 24

HG High Gain. 22

HGHG High Gain – High Gain. 24

HGLG Hig Gain – Low Gain. 24

HL-LHC High Luminosity LHC. 14

HLT High Level Trigger. 18

IBL Insertable B-Layer. 14

ID Inner Detector. 13

IP interaction point. 11

ITC Intermediate Tile Calorimeter. 21

L1 Level One. 18

LAr Liquid Argon. 15

LB Long Barrel. 21

LFN Low Frequency Noise. 24

LG Low Gain. 22

LGHG Low Gain – High Gain. 24

LGLG Low Gain – Low Gain. 24

LHC Large Hadron Collider. 11

LUCID LUminosity measurement using Cerenkov Integrating Detector. 16

LVPS Low Voltage Power Supply. 24

MC Monte Carlo. 24

MDT Monitored Drift Tubes. 16

MS Muon Spectrometer. 16

OF Optimal Filtering. 22

OR Overlap Removal. 27

PMT PhotoMultiplier Tube. 20

PS Proton Synchrotron. 11

PSB Proton Synchrotron Booster. 11

PV Primary Vertex. 27

RMS Root Mean Square. 23

ROD ReadOut Driver. 22

RoIs Region of Interest. 18

RPC Resistive Plate Chambers. 16

SA Stand Alone. 29

SCT SemiConductor Tracker. 14

SPS Super Proton Synchrotron. 11

ST Segment Tagged. 29

TGC Thin Gap Chamber. 16

TileCal Tile Calorimeter. 15

TRT Transition Radiation Tracker. 14

TST Track Soft Term. 29

WSF Wavelength Shifting Fibers. 22

ZDC Zero-Degree Calorimeter. 16

Bibliography

[1] F. Halzen and A. D. Martin. *Quark and Leptons: An introductory Course in Moderm Particle Physics*. John Wiley & Sons INC, 1984.

[2] G. 't Hooft. *Recent Developments in Gauge Theories*. Plenum Press, 1979.

[3] Gian Francesco Giudice. "Naturally Speaking: The Naturalness Criterion and Physics at the LHC". In: (2008). arXiv: 0801.2562 [hep-ph].

[4] Lyndon R Evans and Philip Bryant. "LHC Machine". In: *J. Instrum.* 3 (2008). This report is an abridged version of the LHC Design Report (CERN-2004-003), S08001. 164 p. URL: https://cds.cern.ch/record/1129806.

[5] The ATLAS Collaboration. "The ATLAS Experiment at the CERN Large Hadron Collider". In: *Journal of Instrumentation* 3.08 (2008), S08003. URL: http://stacks.iop.org/1748-0221/3/i=08/a=S08003.

[6] The CMS Collaboration. "The CMS experiment at the CERN LHC". In: *Journal of Instrumentation* 3.08 (2008), S08004. URL: http://stacks.iop.org/1748-0221/3/i=08/a=S08004.

[7] M Capeans et al. *ATLAS Insertable B-Layer Technical Design Report*. Tech. rep. CERN-LHCC-2010-013. ATLAS-TDR-19. Geneva: CERN, Sept. 2010. URL: http://cds.cern.ch/record/1291633.

[8] C. W. Fabjan and F. Gianotti. "Calorimetry for particle physics". In: *Rev. Mod. Phys.* 75 (2003), pp. 1243–1286. DOI: 10.1103/RevModPhys.75.1243.

[9] Aranzazu Ruiz-Martinez and ATLAS Collaboration. *The Run-2 ATLAS Trigger System*. Tech. rep. ATL-DAQ-PROC-2016-003. Geneva: CERN, Feb. 2016. URL: https://cds.cern.ch/record/2133909.

[10] *ATLAS tile calorimeter: Technical Design Report*. Technical Design Report ATLAS. Geneva: CERN, 1996. URL: https://cds.cern.ch/record/331062.

[11] B S M Peralva et al. *The TileCal Energy Reconstruction for Collision Data Using the Matched Filter*. Tech. rep. ATL-TILECAL-PROC-2013-023. Geneva: CERN, Nov. 2013. URL: http://cds.cern.ch/record/1629575.

[12] W Lampl et al. *Calorimeter Clustering Algorithms: Description and Performance*. Tech. rep. ATL-LARG-PUB-2008-002. ATL-COM-LARG-2008-003. Geneva: CERN, Apr. 2008. URL: https://cds.cern.ch/record/1099735.

[13] G. Aad et al. "Readiness of the ATLAS Tile Calorimeter for LHC collisions". In: *Eur. Phys. J.* C70 (2010), pp. 1193–1236. DOI: 10.1140/epjc/s10052-010-1508-y. arXiv: 1007.5423 [physics.ins-det].

[14] G. Bertoli. *Private conversation with Alexander Solodcov*. unpublished. 2014.

[15] G Piacquadio, K Prokofiev, and A Wildauer. "Primary vertex reconstruction in the ATLAS experiment at LHC". In: *Journal of Physics: Conference Series* 119.3 (2008), p. 032033. URL: http://stacks.iop.org/1742-6596/119/i=3/a=032033.

[16] John Alison and I. J. Kroll. "The Road to Discovery: Detector Alignment, Electron Identification, Particle Misidentification, WW Physics, and the Discovery of the Higgs Boson". Presented 08 Nov 2012. PhD thesis. Pennsylvania U.: Pennsylvania U., Dec. 2012. URL: https://cds.cern.ch/record/1536507.

[17] *Electron identification measurements in ATLAS using $\sqrt{s} = 13$ TeV data with 50 ns bunch spacing*. Tech. rep. ATL-PHYS-PUB-2015-041. Geneva: CERN, Sept. 2015. URL: https://cds.cern.ch/record/2048202.

[18] The ATLAS Collaboration. *Muon reconstruction performance in early $\sqrt{s} = 13$ TeV data*. Tech. rep. ATL-PHYS-PUB-2015-037. Geneva: CERN, Aug. 2015. URL: https://cds.cern.ch/record/2047831.

[19] Benjamin Hylton Brunt et al. *Expected performance of missing transverse momentum reconstruction for the ATLAS detector at $\sqrt{s} = 13$ TeV*. Tech. rep. ATL-COM-PHYS-2015-347. Geneva: CERN, May 2015. URL: https://cds.cern.ch/record/2013489.

[20] Matteo Cacciari, Gavin P. Salam, and Gregory Soyez. "The Anti-k(t) jet clustering algorithm". In: *JHEP* 04 (2008), p. 063. DOI: 10.1088/1126-6708/2008/04/063. arXiv: 0802.1189 [hep-ph].

[21] *Pile-up subtraction and suppression for jets in ATLAS*. Tech. rep. ATLAS-CONF-2013-083. Geneva: CERN, Aug. 2013. URL: https://cds.cern.ch/record/1570994.

[22] *Tagging and suppression of pileup jets with the ATLAS detector*. Tech. rep. ATLAS-CONF-2014-018. Geneva: CERN, May 2014. URL: http://cds.cern.ch/record/1700870.

[23] Marianna Testa. "Performance of pile-up mitigation techniques for jets in pp collisions with the ATLAS detector". In: (June 2015). URL: https://cds.cern.ch/record/2022887.

[24] *Measurement of the jet mass scale and resolution uncertainty for large radius jets at $\sqrt{s} = 8$ TeV using the ATLAS detector*. Tech. rep. ATLAS-CONF-2016-008. Geneva: CERN, Mar. 2016. URL: https://cds.cern.ch/record/2139642.

[25] *Jet energy scale and its systematic uncertainty in proton-proton collisions at sqrt(s)=7 TeV in ATLAS 2010 data*. Tech. rep. ATLAS-CONF-2011-032. Geneva: CERN, Mar. 2011. URL: http://cds.cern.ch/record/1337782.

[26] *Selection of jets produced in 13TeV proton-proton collisions with the ATLAS detector*. Tech. rep. ATLAS-CONF-2015-029. Geneva: CERN, July 2015. URL: https://cds.cern.ch/record/2037702.

[27] K. A. Olive et al. "Review of Particle Physics". In: *Chin. Phys.* C38 (2014), p. 090001. DOI: 10.1088/1674-1137/38/9/090001.